Invariant states in inclined layer convection. Part 2. Bifurcations and connections between branches of invariant states

FLORIAN REETZ[1] **PRIYA SUBRAMANIAN**[2,3] **& TOBIAS M. SCHNEIDER**[1]†

[1] Emergent Complexity in Physical Systems Laboratory (ECPS), Ecole Polytechnique Fédérale de Lausanne, CH-1015, Switzerland
[2] School of Mathematics, University of Leeds, Leeds LS2 9JT, UK
[3] Mathematical Institute, University of Oxford, Woodstock Road, Oxford OX2 6GG, UK

(Received ?? and in revised form ??)

Convection in a layer inclined against gravity is a thermally driven non-equilibrium system, in which both buoyancy and shear forces drive spatio-temporally complex flow. As a function of the strength of thermal driving and the angle of inclination, a multitude of convection patterns is observed in experiments and numerical simulations. Several observed patterns have been linked to exact invariant states of the fully nonlinear 3D Oberbeck-Boussinesq equations. These exact equilibria, traveling waves and periodic orbits reside in state space and, depending on their stability properties, are transiently visited by the dynamics or act as attractors. To explain the dependence of observed convection patterns on control parameters, we study the parameter dependence of the state space structure. Specifically, we identify the bifurcations that modify the existence, stability and connectivity of invariant states. We numerically continue exact invariant states underlying spatially periodic convection patterns at $\mathrm{Pr} = 1.07$ under changing control parameters for temperature difference between the walls and inclination angle. The resulting state branches cover various inclinations from horizontal layer convection to vertical layer convection and beyond. The collection of all computed branches represents an extensive bifurcation network connecting 16 different invariant states across control parameters. Individual bifurcation structures are discussed in detail and related to the observed complex dynamics of individual convection patterns. Together, the bifurcations and associated state branches indicate at what control parameters which invariant states coexist. This provides a nonlinear framework to explain the multitude of complex flow dynamics arising in inclined layer convection.

1. Introduction

Thermal convection in a gap between two parallel infinite walls maintained at different fixed temperatures, a system known as Rayleigh-Bénard convection, is a thermally driven nonequilibrium system that exhibits many different complex convection patterns (e.g. Cross & Greenside 2009). When inclining the walls against gravity, hot and cold fluid flows up and down the incline, respectively, creating a cubic laminar flow that breaks the isotropy of a horizontal layer and produces shear forces. This system is known as inclined layer convection (ILC). ILC has three control parameters: the temperature difference

† Email address for correspondence: tobias.schneider@epfl.ch

between the walls, the Prandtl number Pr parametrising the diffusive properties of the fluid, and the angle of inclination against gravity.

Recent experiments of ILC using compressed CO_2 ($\mathrm{Pr} = 1.07$) have systematically varied the temperature difference and the inclination angle over a wide range, and report ten different spatio-temporal convection patterns (Daniels *et al.* 2000). In these experiments, the flow domain has a lateral extent much larger than the gap height and thereby allows large-scale patterns to form. The observed convection patterns show spatio-temporally complex dynamics. This includes intermittent temporal bursting of spatially localized convection structures, observed both at small angles of inclination (Busse & Clever 2000; Daniels *et al.* 2000) as well as at large angles of inclination (Daniels *et al.* 2003). Other examples include transient oblique patterns forming unsteady interfaces between spatial domains of differently oriented wavy roll patterns (Daniels & Bodenschatz 2002; Daniels *et al.* 2008), bimodal patterns, turbulent patterns like crawling rolls at intermediate inclinations (Daniels *et al.* 2008) and chaotically switching diamond panes. These convection patterns have also been reproduced in direct numerical simulations of ILC (Subramanian *et al.* 2016). How the large variety of patterns at different control parameters emerges from the nonlinear equations describing the flow is however not completely understood.

Theoretical approaches towards explaining spatio-temporal convection patterns in ILC can be described as either an approach 'close to thresholds' or an approach 'far above thresholds'. Approaches 'close to thresholds' include linear stability analysis and the construction of weakly nonlinear amplitude equations. At critical stability thresholds, flow states become unstable and give rise to new pattern motifs. Linear stability analysis of laminar ILC (Gershuni & Zhukhovitskii 1969; Vest & Arpaci 1969; Hart 1971; Ruth *et al.* 1980; Chen & Pearlstein 1989; Fujimura & Kelly 1993) identified two different types of primary instabilities. A buoyancy driven instability gives rise to straight convection rolls oriented along the base flow at small inclinations. A shear driven instability gives rise to straight convection rolls oriented transverse to the base flow at large inclinations. Secondary instabilities of finite amplitude straight convection rolls and subsequent tertiary instabilities at increased temperature difference and certain angles of inclination have been investigated using Floquet analysis of two- and three-dimensional states (Clever & Busse 1977; Busse & Clever 1992; Clever & Busse 1995; Busse & Clever 1996; Subramanian *et al.* 2016). Such stability analysis can only explain the onset of convection patterns at, or very close, to the critical stability thresholds in control parameters.

Theoretical approaches to convection patterns 'far above thresholds' include the construction of finite amplitude states within a nonlinear analysis at control parameters far above the critical stability thresholds. Finite amplitude states can be constructed by choosing a Galerkin projection for the governing equations of ILC, often motivated by pattern motifs and their symmetries as identified in a stability analysis at critical stability thresholds (Busse & Clever 1996; Golubitsky & Stewart 2002). Galerkin approximations can then be evolved in time under the fully nonlinear governing equations until their amplitudes saturate at finite values with either steady or periodic time evolution (Subramanian *et al.* 2016). Alternative to forward time integration, finite amplitudes of a Galerkin projection may also be calculated using a Newton-Raphson iteration giving access also to dynamically unstable finite amplitude states (Busse & Clever 1992; Fujimura & Kelly 1993; Subramanian *et al.* 2016). If Galerkin projections invoke a complete basis and fully resolve all spatial scales and modal interactions in the three-dimensional flow, exact finite-amplitude states with steady or periodic time evolution can be found. These so-called invariant states are time-invariant exact solutions of the full nonlinear partial differential equations governing the flow. Depending on their temporal dynamics, invariant states are steady equilibrium states, traveling waves or periodic orbits, all of

which capture particular structures in the flow. Invariant states can either be dynamically stable or dynamically unstable. In subcritical shear flows like pipe or Couette flow, the construction and analysis of unstable invariant states has lead to significant progress in understanding the complex dynamics of weakly turbulent flow by describing chaotic state space trajectories relative to invariant states (Kerswell 2005; Eckhardt *et al.* 2007; Kawahara *et al.* 2012, and references therein).

In ILC, only few highly resolved three-dimensional invariant states had been constructed (Busse & Clever 1992; Clever & Busse 1995) before Reetz & Schneider (2019, referred to as RS19 in the following) identified stable and unstable invariant states underlying various convection patterns at $\mathrm{Pr} = 1.07$ observed in experiments (Daniels *et al.* 2000) and simulations (Subramanian *et al.* 2016). These invariant states are found to transiently attract and repel the dynamics of ILC that is numerically simulated in minimal periodic domains. Minimal periodic domains accommodate only a single spatial period of a periodic convection pattern. Any invariant state computed in minimal periodic domains is also an invariant state in larger extended domains where the pattern of the state periodically repeats in space. To capture a specific pattern with an invariant state in a minimal periodic domain, the size of the domain must be chosen appropriately to match the wavelengths of the pattern. A suitable domain size for a specific pattern can be suggested by Floquet analysis which determines the most unstable pattern wavelength of an instability. At the critical thresholds of instabilities, invariant states emerge in bifurcations and may continue as state branches far above critical thresholds. Thus, bifurcations provide a connection between instabilities 'at thresholds' and invariant states 'far above thresholds'.

In general, bifurcations are structural changes in a system's state space across which the dynamics of the system changes qualitatively (Guckenheimer & Holmes 1983). Emerging stable invariant states that may continue 'far above thresholds' correspond to a supercrtical, forward bifurcation leading to continuous changes in the dynamics. Subcritical bifurcations however, create discontinuous changes in the dynamics allowing for sudden transitions from one state of the system to a very different state. Prominent and potentially harmful examples of such bifurcations, also called tipping points, have been identified in the earth's climate system (Lenton *et al.* 2008) or in combustion chambers (Juniper & Sujith 2018). In low-dimensional nonlinear model systems, like the three-dimensional Lorenz model for thermal convection (Lorenz 1963), various types of bifurcations have been found and related to different routes to chaos (see Argyris *et al.* 1993, for a review). Thus, different types of bifurcations change the dynamics in different ways. Complex temporal dynamics may be observed where invariant states coexist at equal control parameters (RS19). Complex spatial dynamics, like spatial coexistence of different states in a non-conservative system as ILC, suggests that the spatially coexisting states also coexist as individual states at equal control parameters (Knobloch 2015). Coexistence of invariant states at equal control parameters is a consequence of bifurcations creating these invariant states. Thus, bifurcations creating invariant states that underlie observed convection patterns in ILC not only provide a parametric connection between invariant states and instabilities, but may also explain the state space structure underlying the spatio-temporally complex dynamics observed in spatially extended domains.

Computing bifurcation diagrams in nonlinear dynamical systems requires in practice to numerically continue branches of stable and unstable invariant states under changes of control parameters (see Dijkstra *et al.* 2014, for a review). Numerically fully resolved invariant states in minimal periodic domains of ILC have between $\sim 10^4$ and $\sim 10^6$ degrees of freedom (RS19), fewer than the earth's climate system but much more than the Lorenz equations. Due to the numerically demanding size of the state space, not many

prior studies have computed bifurcation diagrams in ILC. Using 4 degrees of freedom, Fujimura & Kelly (1993) traced states of mixed longitudinal and transverse modes in almost vertical fluid layers. Using $\sim 10^3$ degrees of freedom, Busse & Clever (1992) continued invariant states underlying three-dimensional wavy rolls at selected Pr and angles of inclinations, and Clever & Busse (1995) followed a sequence of supercritical bifurcations in vertical fluid layers. Bifurcation diagrams of two-dimensional invariant states have been computed in vertical convection (Mizushima & Tanaka 2002*a*,*b*) and horizontal convection (Waleffe *et al.* 2015), not addressing three-dimensional dynamics. Recent advances in matrix-free algorithms and computer hardware allow to efficiently construct and continue fully resolved three-dimensional invariant states in double-periodic domains with channel geometry (Viswanath 2007; Gibson *et al.* 2008). We use an extension to the existing numerical framework of the MPI-parallel code *Channelflow 2.0* (Gibson *et al.* 2019) that also handles ILC (RS19).

The aim of this paper is to systematically compute and describe bifurcations in ILC. These bifurcations explain the spatio-temporal complexity observed both experimentally and numerically. Using numerical continuation, we trace invariant states that have been constructed in RS19 and that underlie the observed basic convection patterns. The analysis covers the same range of system parameters as recent experimental (Daniels *et al.* 2000) and theoretical work (Subramanian *et al.* 2016) at $\mathrm{Pr} = 1.07$ and leads to an extensive network of bifurcating branches across control parameters. To understand how temporal and spatio-temporal complexity arises in ILC, we specifically address the following three questions:

Q1 Bifurcation types: Complex temporal dynamics between coexisting invariant states is a result of bifurcations creating the associated invariant states. Different bifurcation types change the dynamics in different ways. What types of bifurcations create invariant states underlying the observed convection patterns in ILC?

Q2 Connection to instabilities: Floquet analysis characterises instabilities at critical control parameters. Results from such an analysis are valid close to the critical thresholds for small amplitude solutions. Do the fully nonlinear invariant states, found in RS19 to underlie the observed convection patterns far from critical thresholds in ILC, bifurcate at the corresponding secondary instabilities reported from a Floquet analysis in Subramanian *et al.* (2016)?

Q3 Range of existence: Spatio-temporally complex dynamics suggests existence of invariant states at the associated control parameters. How do the bifurcation branches of invariant states in ILC continue across control parameters and what are the limits of their existence?

The present article is structured in the following way. Section 2 describes the numerical methods and outlines the systematic bifurcation analysis. The results of the bifurcation analysis are stated in Section 3. In five subsections, we report in detail on selected bifurcation diagrams explaining individual convection patterns. The results are discussed in response to *Q1*-*Q3* in Section 4.

2. Bifurcation analysis of invariant states

Before introducing the approach of the bifurcation analysis in Section 2.3, we summarize the basic numerical concepts underlying direct numerical simulations of ILC (Section

2.1), and describe the invariant states that capture relevant convection patterns (Section 2.2). More details on the direct numerical simulations and identified invariant states are described elsewhere (RS19).

2.1. *Direct numerical simulation of inclined layer convection*

ILC is studied by numerically solving the nondimensionalised Oberbeck-Boussinesq equations for the velocity $\boldsymbol{U}$, temperature $\mathcal{T}$ and pressure p relative to the hydrostatic pressure

$$\frac{\partial \boldsymbol{U}}{\partial t} + (\boldsymbol{U}\cdot\nabla)\,\boldsymbol{U} = -\nabla p + \tilde{\nu}\nabla^2\boldsymbol{U} - \hat{\boldsymbol{g}}\,\mathcal{T}\ , \tag{2.1}$$

$$\frac{\partial \mathcal{T}}{\partial t} + (\boldsymbol{U}\cdot\nabla)\,\mathcal{T} = \tilde{\kappa}\nabla^2\mathcal{T}\ , \tag{2.2}$$

$$\nabla\cdot\boldsymbol{U} = 0\ , \tag{2.3}$$

in numerical domains with x, y and z indicating the streamwise, the spanwise and the wall-normal dimension. The domains are bounded in z by two parallel walls at $z = \pm 0.5$. In the streamwise dimension x and the spanwise dimension y periodic boundary conditions are imposed at $x = [0, L_x]$ and $y = [0, L_y]$, respectively. The walls are stationary with $\boldsymbol{U}(z = \pm 0.5) = 0$, have prescribed temperatures $\mathcal{T}(z = \pm 0.5) = \mp 0.5$, and are inclined against the gravitational unit vector $\hat{\boldsymbol{g}} = -\sin(\gamma)\boldsymbol{e}_x - \cos(\gamma)\boldsymbol{e}_z$ by inclination angle γ. With these boundary conditions, Equations (2.1-2.3) admit the laminar solution

$$\boldsymbol{U}_0(z) = \frac{\sin(\gamma)}{6\,\tilde{\nu}}\left(z^3 - \frac{1}{4}z\right)\boldsymbol{e}_x\ , \tag{2.4}$$

$$\mathcal{T}_0(z) = -z\ , \tag{2.5}$$

$$p_0(z) = \Pi - \cos(\gamma)z^2/2\ , \tag{2.6}$$

with arbitrary pressure constant Π. Equations (2.1-2.3) are nondimensionalised by three characteristic scales of the system. We have chosen the temperature difference $\Delta\mathcal{T}$ between the walls, the gap height H, and the free-fall velocity $U_f = (g\,\alpha\,\Delta\mathcal{T}H)^{1/2}$ as characteristic scales. This nondimensionalisation defines the parameters $\tilde{\nu} = (\mathrm{Pr}/\mathrm{Ra})^{1/2}$ and $\tilde{\kappa} = (\mathrm{Pr}\,\mathrm{Ra})^{-1/2}$ in terms of the Rayleigh number $\mathrm{Ra} = g\,\alpha\,\Delta T\,H^3/(\nu\kappa)$ and the Prandtl number $\mathrm{Pr} = \nu/\kappa$. Here, α is the thermal expansion coefficient, ν is the kinematic viscosity, and κ is thermal diffusivity. Thus, ILC has three control parameters, γ, Ra, and Pr, of which we fix $\mathrm{Pr} = 1.07$.

Time is measured in free-fall units H/U_f but will also be compared with other relevant time scales of ILC, like the heat diffusion time H^2/κ, and the laminar mean advection time $L_x/\bar{U}_0$. The latter follows from the laminar velocity profile (2.4) integrated over the lower half of the domain where $-0.5 \leqslant z \leqslant 0$, that is $\bar{U}_0 = \sin(\gamma)/384\tilde{\nu}$.

The pseudo-spectral code *Channelflow 2.0* (Gibson *et al.* 2019) has been extended to solve (2.1-2.3) using Fourier-Chebychev-Fourier expansions with N spectral modes in space and a 3rd order implicit-explicit multistep algorithm to march forward in time (see RS19; and references therein). Any time evolution computed with *Channelflow-ILC* represents a unique state vector trajectory $\boldsymbol{x}(t) = [\boldsymbol{u}, \theta](x, y, z, t)$ in a state space with N dimensions. This state space contains all solenoidal velocity fluctuations $\boldsymbol{u} = \boldsymbol{U} - \boldsymbol{U}_0$ and temperature fluctuations $\theta = \mathcal{T} - \mathcal{T}_0$.

2.2. *Computing invariant states*

Invariant states are particular state vectors $\boldsymbol{x}^*(t)$ representing roots of a recurrent map

$$\mathcal{G}(\boldsymbol{x}^*, \mu) = \sigma\mathcal{F}^T(\boldsymbol{x}^*, \mu) - \boldsymbol{x}^* = 0\ . \tag{2.7}$$

Here, $\mathcal{F}^T(\boldsymbol{x},\mu)$ is the dynamical map integrating (2.1-2.3) from state $\boldsymbol{x}$ over time period T at system parameter $\mu \in [\gamma, \mathrm{Ra}, \mathrm{Pr}]$. The invariant state is either an equilibrium state if T is a free parameter, or a periodic orbit if T must match a specific period. Definition (2.7) includes a symmetry transformation $\sigma \in S_{ilc}$. The symmetry group $S_{ilc} = O(2)_x \times O(2)_y$, where $\times$ is the direct product, is an equivariance of Equations (2.1-2.3) in x-y-periodic domains. S_{ilc} is generated by spanwise y-reflection π_y, streamwise x-z-reflection π_{xz}, and x- and y-translations $\tau(a_x, a_y)$ such that

$$\pi_y[u,v,w,\theta](x,y,z) = [u,-v,w,\theta](x,-y,z) \ , \tag{2.8}$$

$$\pi_{xz}[u,v,w,\theta](x,y,z) = [-u,v,-w,-\theta](-x,y,-z) \ , \tag{2.9}$$

$$\tau(a_x,a_y)[u,v,w,\theta](x,y,z) = [u,v,w,\theta](x+a_xL_x, y+a_yL_y, z) \ , \tag{2.10}$$

with shift factors $a_x, a_y \in [0,1)$ scaling the spatial periods L_x and L_y of the periodic domain. All invariant states discussed here are invariant under transformations within subgroups of $S_{ilc} = \langle \pi_y, \pi_{xz}, \tau(a_x,a_y)\rangle$, where angle brackets $\langle\rangle$ imply all products of elements given in the brackets. The specific coordinate transformations for reflection symmetries depend on the spatial phase of the flow structure relative to the origin. We choose the spatial phase such that three-dimensional inversion $\pi_{xyz} = \pi_y\pi_{xz}$, where applicable to invariant states, applies with respect to the domain origin at $(x,y,z) = (0,0,0)$.

If $\sigma \neq 1$ in (2.7), the invariant state is a *relative* invariant state. A traveling wave state, where $\sigma = \tau(a_x,a_y)$ with specific shift factors a_x and a_y, is a relative equilibrium state. A relative periodic orbit is either traveling, where $\sigma = \tau(a_x,a_y)$ must be applied after period T, or is 'pre-periodic' if $\sigma = 1$ after a full period T but $\sigma \neq 1$ after time interval $T' = T/n$ with $n \in \mathbb{N}$.

Invariant states are computed by solving (2.7) with a Newton-Raphson iteration using matrix-free Krylov methods (Gibson *et al.* 2019). Practically, we stop iterations if $||\mathcal{G}(\boldsymbol{x},\mu)||_2 < 10^{-13}$ where

$$||\boldsymbol{x}||_2 = \left(\frac{1}{L_xL_y} \int_0^{L_x}\int_0^{L_y}\int_{-0.5}^{0.5} u^2+v^2+w^2+\theta^2 dx\,dy\,dz \right)^{1/2} \ . \tag{2.11}$$

A residual of $< 10^{-13}$ is sufficiently close to double machine precision to consider the iteration as fully converged.

Invariant states may be dynamically stable or unstable. The dynamical stability is characterised by the eigenvalues and eigenmodes of the linearised equations computed using Arnoldi iteration (Gibson *et al.* 2019) and depends on the specific symmetry subspace defined by size $[L_x, L_y]$ of the periodic domain and potentially imposed discrete symmetries $\sigma \in S_{ilc}$. We impose σ on a state vector $\boldsymbol{x}(t)$ using a projection $(\boldsymbol{x}(t) + \sigma\boldsymbol{x}(t))/2$ which requires $\sigma^2 = 1$. We will specify the considered symmetry subspace for each computation of the eigenvalue spectrum.

Previously, invariant states underlying observed convection patterns in ILC have been identified by combining direct numerical simulations in small periodic domains with Newton-Raphson iteration (RS19). There, simulations from unstable laminar flow perturbed by small-amplitude noise lead to temporal transitions between seven invariant states. All of these seven invariant states are either stable or weakly unstable, depending on the symmetry subspace corresponding to the chosen periodic domain, control parameters and potentially imposed discrete symmetries. As a consequence, the temporal dynamics is either asymptotically or transiently attracted to these invariant states. Moreover, the temporal dynamics is found to visit these invariant states in a specific

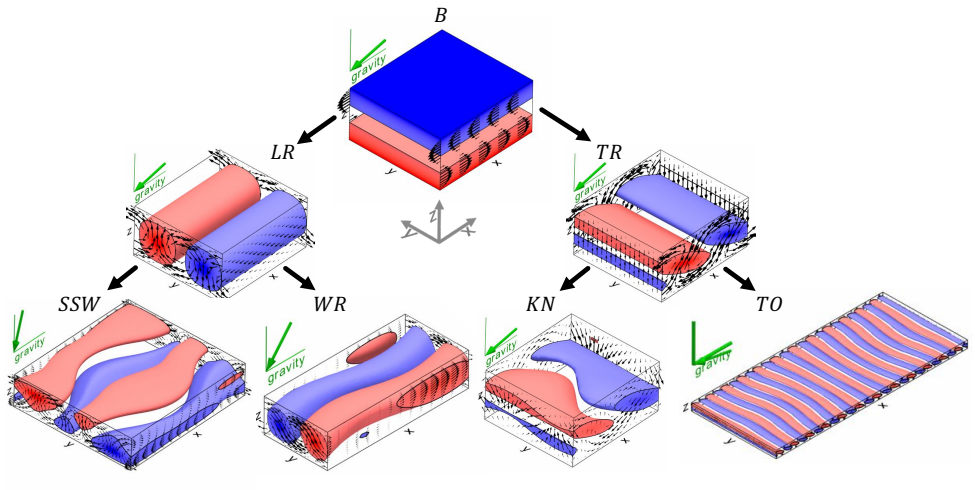

Figure 1: Invariant states found as sequentially visited states in temporal transitions at selected control parameters (RS19). Black arrows indicate the direction of temporal transitions, starting from laminar base flow B, via longitudinal and transverse rolls (equilibria LR and TR), to four different tertiary invariant states representing the convection patterns of subharmonic standing waves (periodic orbit SSW), wavy rolls (equilibrium WR), knots (equilibrium KN) and transverse oscillations (periodic orbit TO). While B is shown as the vector fields of total velocity $\boldsymbol{U}$ at the box sides and 3D contours of total temperature $\mathcal{T}$, all other states are shown in terms of velocity and temperature fluctuations, $\boldsymbol{u}$ and θ, around B. Iso-contours of temperature are at $1/3[\min(\theta), \max(\theta)]$. The states are computed at different inclinations of the domain (green gravity vectors): B, LR and TR at γ_{c2}, and the four tertiary states at the system parameters marked in Figure 2.

sequential order. Figure 1 summarizes the observed transition sequences and visualises the flow structures of all seven invariant states. Which invariant state is visited by the dynamics depends on the control parameters. Following Daniels *et al.* (2000) and Subramanian *et al.* (2016), we explore the two-dimensional parameter space of inclination angle γ and Rayleigh number Ra at fixed Pr $= 1.07$. Here, a codimension-2 point at $[\gamma_{c2}, \mathrm{Ra}_{c2}]$ determines the type of primary instability and visited secondary state. In general, at any Prandtl number, the transition from a laminar base flow (B) leads to longitudinal rolls (LR) for angles of $\gamma < \gamma_{c2}$, while for angles with $\gamma > \gamma_{c2}$ the transition from B leads to transverse rolls (TR). At Pr $= 1.07$, we determine the codimension-2 point accurately at $[\gamma_{c2}, \mathrm{Ra}_{c2}] = [77.7567°, 8053.1]$ when computing LR and TR in a domain with periodicity $[L_x, L_y] = [\lambda_x, \lambda_y]$ where $[\lambda_x, \lambda_y] = [2.2211, 2.0162]$ and grid size $[n_x, n_y, n_z] = [32, 32, 25]$. Wavelengths λ_x and λ_y are suggested by Floquet analysis (Subramanian *et al.* 2016). As in RS19, we fix the domain periodicity $[\lambda_x, \lambda_y]$ and the grid resolution $[n_x, n_y, n_z]$ throughout this study and choose all computational domains as multiples of this minimal periodic box. Subharmonic standing waves (SSW) are computed in a domain with periodicity $[L_x, L_y] = [2\lambda_x, 2\lambda_y]$, wavy rolls ($WR$) with $[L_x, L_y] = [2\lambda_x, \lambda_y]$, knots ($KN$) with $[L_x, L_y] = [\lambda_x, \lambda_y]$, and transverse oscillations (TO) with $[L_x, L_y] = [12\lambda_x, 6\lambda_y]$. The grid size is scaled accordingly. Choosing all do-

mains as integer multiples of the same minimal box ensures commensurable wavelengths and thus allows for potential bifurcation between invariant states.

The approach of combining direct numerical simulations from unstable laminar flow with Newton-Raphson iteration allows to determine all of the above invariant states. However, this approach fails in the case of the pattern emerging from the skewed varicose instability at $\gamma = 0°$ (RS19). There, the dynamics does not asymptotically approach or transiently visit an invariant state underlying the pattern, suggesting that no associated invariant state exists above thresholds. Therefore, we search for the bifurcating branch below critical parameters of the skewed varicose instability by taking the following steps. The bifurcating eigenmode that destabilizes x-aligned straight convection rolls at wavelength λ_y ($R_{\lambda 2}$) in a domain of periodicity $[L_x, L_y] = [4\lambda_x, 4\lambda_y]$ is computed using Arnoldi iteration. Different finite amplitude perturbations of $R_{\lambda 2}$ with the bifurcating eigenmode are integrated forward in time to generate a large set of initial states for brute-force Newton-Raphson iterations below critical threshold parameters of the instability. Using this approach we identified an unstable equilibrium state that underlies the skewed varicose pattern and is described in Section 3.1. Consequently, invariant states in thermal convection cannot be assumed to generically exist above critical control parameters, but may also be found below thresholds suggesting a backward bifurcation. Whether bifurcations are forward or backward in control parameters, is studied in the present bifurcation analysis.

2.3. *Bifurcation analysis*

The general approach of our bifurcation analysis is to compute bifurcation branches of invariant states in ILC and to characterize the resulting bifurcation diagrams. Branches of invariant states are computed using continuation methods to solve (2.7) under a changing control parameter μ (Dijkstra *et al.* 2014). There are two iterative predictor-corrector schemes for numerical continuation implemented in *Channelflow-ILC*. The control parameter continuation uses quadratic extrapolation to predict a state vector $\boldsymbol{x}$ for some value of μ which is fixed in the following Newton-Raphson iteration, the corrector step. The pseudo-arclength continuation does not prescribe μ in the corrector step but solves for μ as additional unknown entry in state vector $\boldsymbol{x}$ under an additional arclength constraint. Depending on the shape of the continued state branch, one continuation scheme might outperform the other (Gibson *et al.* 2019). Continuation of periodic orbits with long periods may require a multi-shooting method to converge (Gibson *et al.* 2019). Where invariant states have discrete reflection symmetries π_y or π_{xz} (2.8-2.9) we impose reflections during numerical continuation because they fix the spatial phase of the flow relative to the x- or y-coordinates. If the spatial phase is free, states may translate under numerical continuation reducing the computational efficiency. Since both continuation schemes solve (2.7) and the algorithmic details do not change the resulting bifurcation diagrams, we use the better performing scheme for each branch.

Continuations of the invariant states cover *a priori* chosen sections across the considered parameter space at $\mathrm{Pr} = 1.07$ covering $0° \leqslant \gamma < 120°$ and $0 \leqslant \epsilon \leqslant 2$, as illustrated by thin grey lines in Figure 2. The control parameter $\epsilon = (\mathrm{Ra} - \mathrm{Ra}_c(\gamma))/\mathrm{Ra}_c(\gamma)$ indicates Ra normalised by a critical threshold function $\mathrm{Ra}_c(\gamma)$ which here, approximates the true critical control parameters $\mathrm{Ra}_c'(\gamma)$ of the primary instability in ILC (see Figure 2a in RS19). Thus, the primary instability defining the onset of convection is always at $\epsilon \approx 0$, independent of the inclination angle. Critical thresholds of bifurcation points are denoted as ϵ_c. To continue invariant states in γ at $\epsilon = \text{const.}$, also Ra needs to be adjusted accounting for variations in $\mathrm{Ra}_c(\gamma)$. Since the true critical $\mathrm{Ra}_c'(\gamma)$ cannot be expressed in

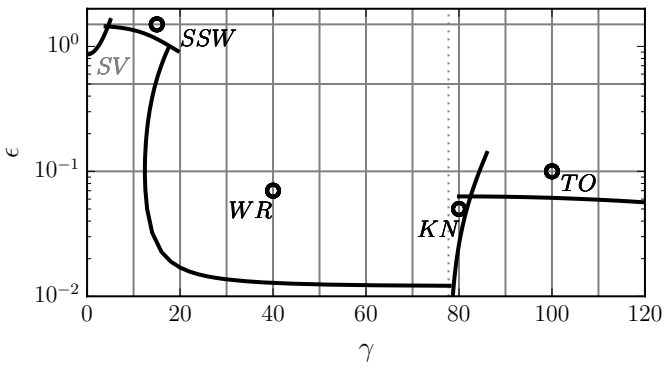

Figure 2: The considered parameter space is spanned by inclination angle γ and $\epsilon = (\mathrm{Ra} - \mathrm{Ra}_c)/\mathrm{Ra}_c$ at $\mathrm{Pr} = 1.07$. The parameters at which invariant states have been identified in RS19 (Figure 1) are marked by circles. The invariant state underlying skewed varicose pattern (SV) is not described in RS19 but identified in this work. Thick solid lines indicate critical thresholds in control parameters of the five secondary instabilities determined by Subramanian *et al.* (2016). Bifurcations between invariant states are computed along 15 sections across the parameter space (grey solid lines). The thin grey dotted line marks the inclination angle of the codimension-2 point at $\gamma_{c2} = 77.7567°$.

closed-form, we define the function

$$\mathrm{Ra}_c(\gamma \leqslant \gamma_{c2}) = \frac{\mathrm{Ra}'_c(\gamma = 0°)}{\cos(\gamma)} \tag{2.12}$$

$$\mathrm{Ra}_c(\gamma > \gamma_{c2}) = \frac{1}{41}(\gamma - \gamma_{c2})^3 + \frac{5}{14}(\gamma - \gamma_{c2})^2 + 29(\gamma - \gamma_{c2}) + \mathrm{Ra}'_{c2} \tag{2.13}$$

to keep $\epsilon = (\mathrm{Ra} - \mathrm{Ra}_c(\gamma))/\mathrm{Ra}_c(\gamma) = $ const. under γ-continuations. The definition of function $\mathrm{Ra}_c(\gamma)$ has three precise coefficients, namely the critical parameters for horizontal convection $\mathrm{Ra}'_c(\gamma = 0°) = 1707.76$ (Busse 1978) and the codimension-2 point $[\gamma_{c2}, \mathrm{Ra}'_{c2}] = [77.7567°, 8053.1]$. Relation (2.12), already found by Gershuni & Zhukhovitskii (1969), is a geometric consequence of the linear laminar temperature profile. Polynomial (2.13) is a least-square-fit of the empirical critical thresholds for $\gamma_{c2} < \gamma < 120°$ reported in Subramanian *et al.* (2016), and is an approximation of the true $\mathrm{Ra}'_c(\gamma) \approx \mathrm{Ra}_c(\gamma)$. The purpose of defining $\mathrm{Ra}_c(\gamma)$ in (2.12-2.13) is not to most accurately capture the true $\mathrm{Ra}'_c(\gamma)$ but to provide a closed-form function for converting values between Ra and ϵ. The conversion allows γ-continuations at $\epsilon = $ const. and a comparison of the present results with other work reported in terms of a similar ϵ', based on the empirically determined primary instabilities.

Linear stability analysis of invariant states is performed at selected points along continued branches. Under continuation, we consider invariant states in their minimal periodic domain capturing only one spatial period of the pattern. In order to compare the dynamical stability between different invariant states, Arnoldi iterations must be performed in identical symmetry subspaces. This implies using the same periodic domains and imposing the same discrete symmetries for all considered states. Wherever we compute the dynamical stability along selected bifurcation branches, we specifically choose and report the symmetry subspace for the full branch.

Many bifurcation types of vector fields are known (e.g. Guckenheimer & Holmes 1983).

The most common bifurcations we encounter in ILC are pitchfork bifurcations, Hopf bifurcations, saddle-node bifurcation and mutual annhilation of two periodic orbits, all of which are also well-known bifurcations in ordinary differential equations (e.g. Schaeffer & Cain 2016). The two latter types we simply refer to as 'folds'. If bifurcations are not one of these four common types, we provide explicit references that discuss the bifurcation type in detail, as such discussions would be beyond the scope of the present work. When discussing symmetry-breaking bifurcations, the classification into supercritical/subcritical bifurcations refers to a 'more stable'/'less stable' bifurcating branch in comparison to the stability of the coexisting parent branch (Tuckerman & Barkley 1990). The orientation of symmetry-breaking bifurcations along a control parameter μ is given specifically as μ-forward or μ-backward.

3. Results

We first provide an overview of the results from the bifurcation analysis. Considering twelve sections at constant γ and three sections at $\epsilon = \text{const.}$ (Figure 2), we present 15 bifurcation diagrams here in Figures 3 and 4. A complete analysis of all branches in these diagrams is beyond the scope of this paper. Instead in this section, we first summarise the bifurcation diagrams and then focus on selected state branches covering the control parameters where spatio-temporally complex convection patterns are observed and temporal dynamics between invariant states has been studied (RS19). We specifically discuss the branches that bifurcate from straight convection rolls via the five secondary instabilities that were identified by Subramanian *et al.* (2016). These are, skewed-varicose instability, longitudinal subharmonic oscillatory instability, wavy roll instability, knot instability and transverse oscillatory instability. Branches of equilibrium and travelling wave states are plotted in terms of the norm of the temperature fluctuations,

$$||\theta||_2 = \left(\frac{1}{L_x L_y} \int_0^{L_x} \int_0^{L_y} \int_{-0.5}^{0.5} \theta^2(x, y, z, t_\pm) dx\, dy\, dz \right)^{1/2}, \tag{3.1}$$

as a function of the bifurcation parameter. Periodic orbits are illustrated by a pair of branches indicating the minimum and maximum of $||\theta||_2$ over one orbit period, at instances $t_\pm$. Bifurcation branches are labeled inside the diagram with the name of the invariant state. We recommend reading each diagram panel by first identifying the branches of LR and/or TR. In most cases, LR or TR have the largest $||\theta||_2$ and tertiary branches bifurcate to lower $||\theta||_2$. See Figure 3 for bifurcations while varying ϵ and Figure 4 for bifurcations while varying γ.

The ϵ-bifurcations at fixed γ, confirm the common observation that LR and TR always bifurcate in supercritical, ϵ-forward pitchfork bifurcations from the laminar base state. At $\gamma = 0$, longitudinal and transverse rolls are related via symmetries, and we refer to both of them as R_λ, where the subscript indicates the wavelength of the roll pattern. At $0 < \gamma \leqslant 20°$, branches of LR and TR still are very close to each other. Only the LR-branches, defining the onset of convection, are plotted to avoid clutter. At $30° \leqslant \gamma \leqslant 40°$, TR bifurcates outside the considered interval of $0 \leqslant \epsilon \leqslant 2$. At $\gamma \geqslant 50°$, the branches of TR and LR bifurcate again closer to each other. The branches however differ significantly in amplitude and functional form. TR-branches show non-monotonic behaviour in $||\theta||_2$, e.g., a local maximum at $\epsilon = 1.8$ and $\gamma = 90°$. Non-monotonic branches of TR were also computed in vertical convection at $\mathrm{Pr} = 0.71$ (Mizushima & Tanaka 2002*a*,*b*).

LR-branches monotonically increase in $||\theta||_2$ with ϵ. For further increasing ϵ, LR ap-

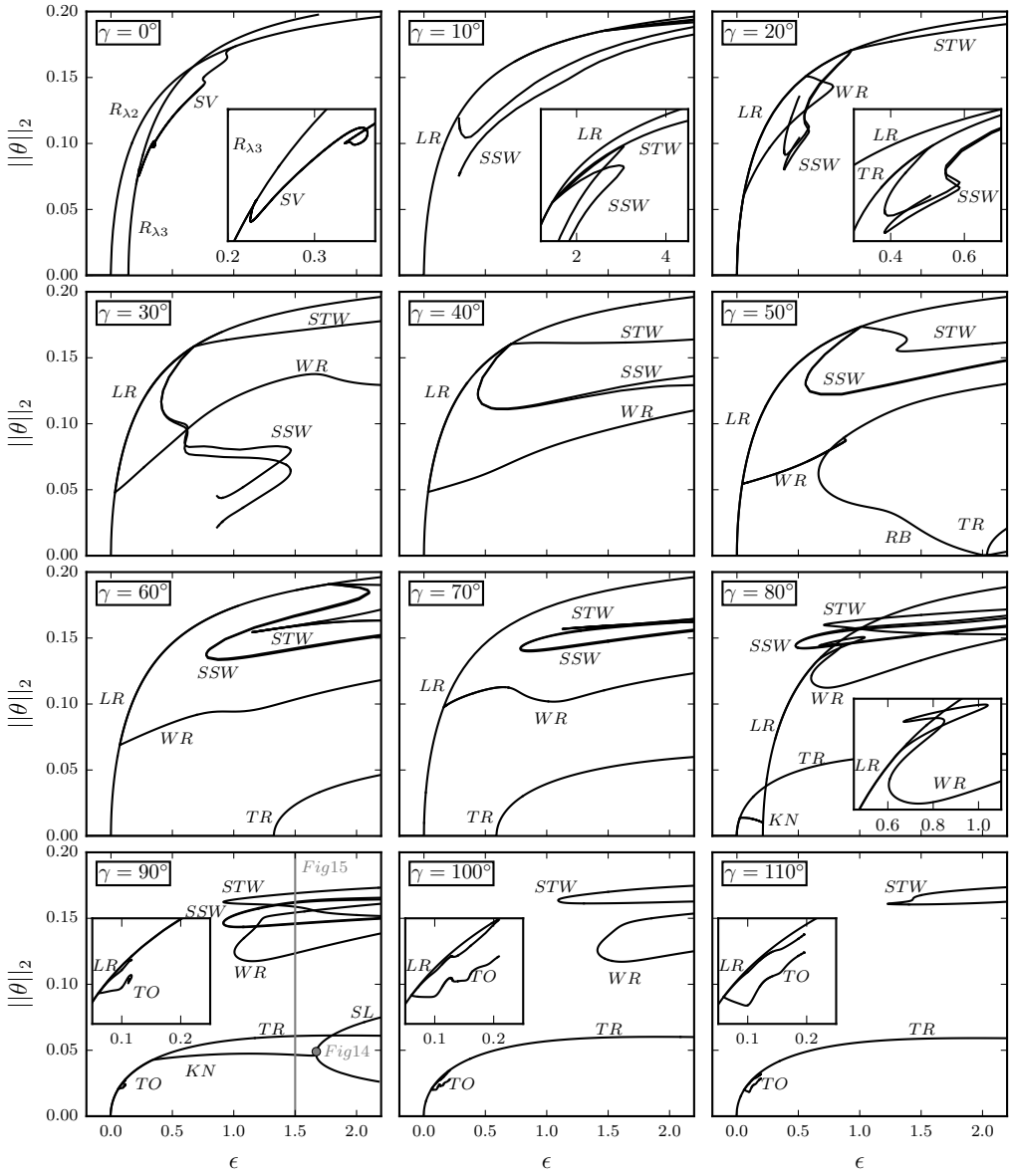

Figure 3: Summary of all bifurcation branches of invariant states continued in ϵ at constant $\gamma \in \{0°, 10°, 20°, ..., 110°\}$. Each branch is plotted in terms of $||\theta||_2$ (Equation 3.1) and is labeled by the name of the invariant state to which the branch belongs. Insets enlarge or isolate features of the bifurcations diagrams. All panels are labeled by the angle of inclination and share the same axes. TR is left out in panels $\gamma \in \{0°, 10°, 20°\}$ to avoid clutter. In panel $\gamma = 90°$, the grey vertical line crosses the bifurcation branches where invariant states are shown in Figure 15 and discussed in Appendix B. KN at $\gamma = 90°$ connect to equilibrium state SL showing a subharmonic lambda pattern (Figure 14), discussed in Appendix A.

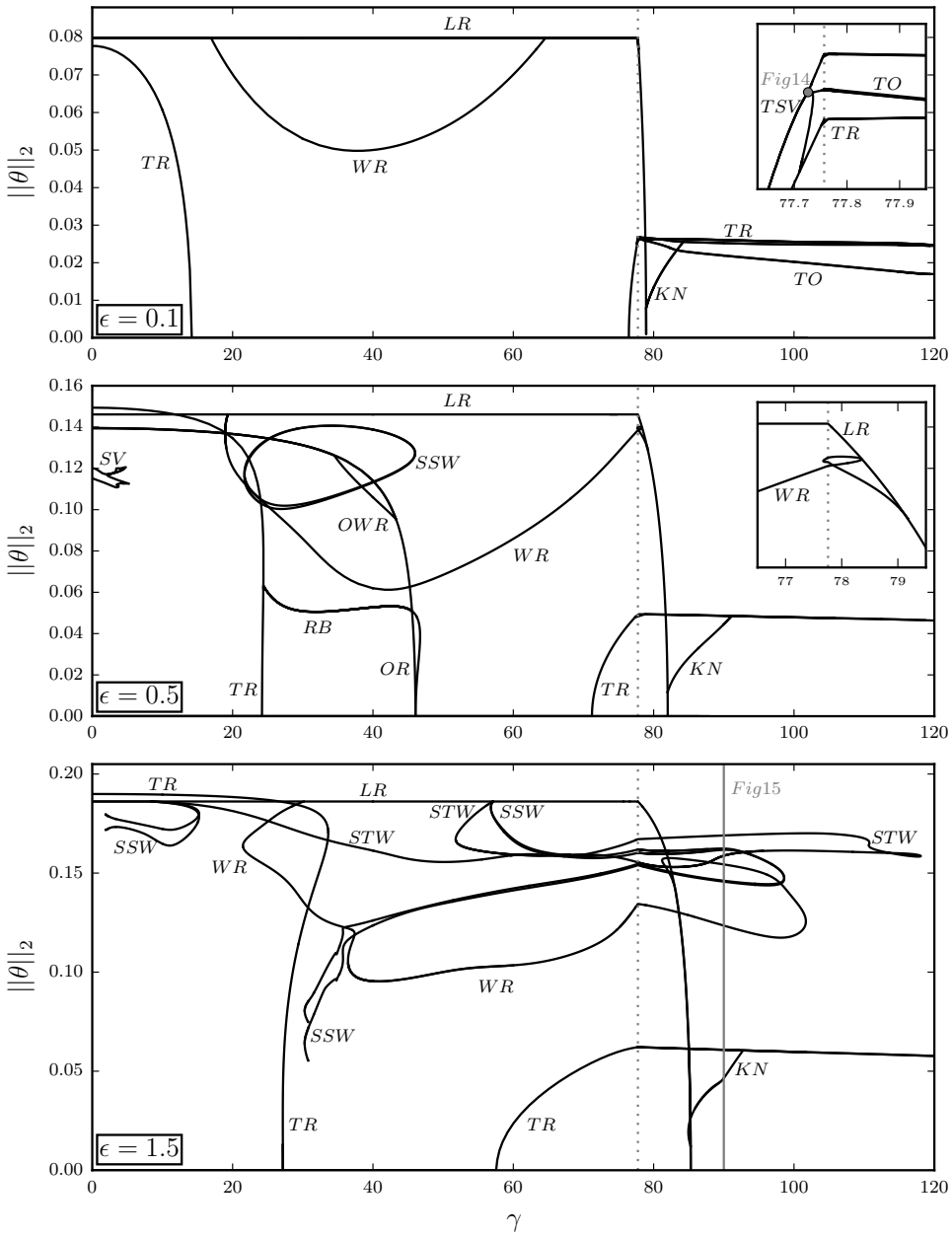

Figure 4: Summary of all bifurcation branches of invariant states continued in γ at constant $\epsilon \in \{0.1, 0.5, 1.5\}$. Each branch is plotted in terms of $||\theta||_2$ (Equation 3.1) and is labeled by the name of the invariant state to which the branch belongs. All panels are labeled by the ϵ value and share the same axes. Grey dotted lines mark the inclination angle of the codimension-2 point. Insets enlarge features of the bifurcations diagrams around the inclination angle of the codimension-2 point. In panel $\epsilon = 1.5$, the grey vertical line crosses the bifurcation branches where invariant states are shown in Figure 15 and discussed in Appendix B. TO at $\epsilon = 0.1$ (inset) connect to equilibrium state TSV showing a transverse subharmonic varicose pattern (Figure 14), discussed in Appendix A.

pears to eventually approach the same ϵ-scaling law as reported for invariant states underlying straight convection rolls in horizontal convection at $\gamma = 0°$ (Waleffe *et al.* 2015). The large-ϵ behaviour is observed for all γ. The observation that a scaling law of straight convection rolls at $\gamma = 0°$ also describes LR-branches at $\gamma \neq 0°$ suggests a particular scaling invariance of the nonlinear Oberbeck-Boussinesq equations under changes of inclination angle γ. This scaling invariance is discussed in the following paragraph.

At fixed ϵ, all γ-continuations of LR result in horizontal lines in $||\theta||_2$ for $0° \leqslant \gamma \leqslant \gamma_{c2}$ (Figure 4). These horizontal lines are a remarkable feature of the bifurcation diagrams and can be explained as a consequence of a scaling invariance of the nonlinear Oberbeck-Boussinesq equations, that holds for patterns or states that are steady in time and uniform in x, like LR:
For $\gamma < \gamma_{c2}$, keeping $\epsilon = \text{const.}$ implies $\text{Ra} \sim 1/\cos(\gamma)$ (2.12). The laminar solution thus scales with γ as $U_0 \sim \sin(\gamma)/\sqrt{\cos(\gamma)}$ and $\mathcal{T}_0 \sim 1$. Here, Pr is constant. Inserting the base-fluctuation decomposition $\boldsymbol{U} = \boldsymbol{U}_0 + \boldsymbol{u}$ and $\mathcal{T} = \mathcal{T}_0 + \theta$ into (2.1-2.3) and assuming $\partial_t[\boldsymbol{u}, \theta] = 0$ and $\partial_x[\boldsymbol{u}, \theta] = 0$ for steady stripe/roll states, the governing equations for each component scale with a global γ-dependent factor, provided that temperature and velocity fluctuations scale as $u(y,z) \sim \sin(\gamma)/\sqrt{\cos(\gamma)}$, $v(y,z) \sim w(y,z) \sim \sqrt{\cos(\gamma)}$, and $\theta(y,z) \sim 1$:

$$
\begin{aligned}
u: \quad & v\partial_y u + w\partial_z(u + U_0(z)) &&= -\partial_x p + (\text{Pr}/\text{Ra})^{1/2}\nabla^2 u + \sin(\gamma)\theta && \sim \sin(\gamma) \quad (3.2)\\
v: \quad & v\partial_y v + w\partial_z v &&= -\partial_y p + (\text{Pr}/\text{Ra})^{1/2}\nabla^2 v && \sim \cos(\gamma) \quad (3.3)\\
w: \quad & v\partial_y w + w\partial_z w &&= -\partial_z p + (\text{Pr}/\text{Ra})^{1/2}\nabla^2 w + \cos(\gamma)\theta && \sim \cos(\gamma) \quad (3.4)\\
\theta: \quad & v\partial_y \theta + w\partial_z(\theta + \mathcal{T}_0(z)) &&= (\text{PrRa})^{-1/2}\nabla^2\theta && \sim \sqrt{\cos(\gamma)} \quad (3.5)\\
c: \quad & \partial_y v + \partial_z w &&= 0 && \sim \sqrt{\cos(\gamma)} \quad (3.6)
\end{aligned}
$$

This scaling implies that any equilibrium at one value of γ corresponds to a whole family of equilibria for $0° \leqslant \gamma \leqslant 90°$. The temperature scaling $\theta(y,z) \sim 1$ directly implies that $||\theta||_2$ of LR remains invariant under changes in γ with $\epsilon = \text{const.}$ This leads to self-similar curves under ϵ-continuation at fixed γ (Figure 3) and horizontal lines under γ-continuation at fixed ϵ (Figure 4). Moreover, any x-uniform and steady invariant state for $0 < \gamma \leqslant 90°$ corresponds to a specific invariant state in the horizontal Rayleigh-Bénard case at $\gamma = 0°$. A similar relation has previously been reported for the infinite Pr limit only (Clever 1973). The scaling relation provided here is valid for all Pr and a property of the full nonlinear Oberbeck-Boussinesq equations.

In the limit of a vertical gap ($\gamma \to 90°$), the $\cos^{-1}(\gamma)$-scaling implies diverging Ra. In this limit, the amplitude of the fixed $u(y,z)$-profile diverges and the cross-flow components vanish, $v, w \to 0$. The temperature field $\theta(y,z)$ remains fixed. Consequently in a vertical gap, hot and cold streamwise jets without cross flow and diverging streamwise velocity amplitude are invariant states in the $\text{Ra} \to \infty$ limit. Any temperature field of LR found at $\gamma < 90°$ is a valid temperature field for these jets at infinite Ra.

The subsequent sections discuss selected bifurcation diagrams covering the parameters where temporal dynamics between invariant states has been studied (RS19). We do not systematically explain the bifurcations at all control parameters but rather highlight important features of the bifurcations at selected control parameters. In each section we summarise key features of the bifurcation structure and relate those to observed spatio-temporally complex dynamics of the flow. The sections are ordered by increasing values of the angle of inclination.

3.1. *Skewed varicose state - subcritical connector of bistable rolls*

The skewed varicose instability of Rayleigh-Bénard convection, first found as spatially periodic instability at Pr = 7 (Busse & Clever 1979), is experimentally observed to trigger a spatially localized transient pattern at Pr = 1.07 with very subtle varicose features (Bodenschatz *et al.* 2000, Figure 7). This section reports on a bifurcation from straight convection rolls to an equilibrium state capturing the observed skewed varicose pattern in a periodic domain. The bifurcating branch is subcritical, exists only below ϵ_c of the skewed varicose instability, and connects two bistable straight convection rolls at different wavelengths and orientations. The subcritical coexistence of the skewed varicose equilibrium with bistable straight convection rolls may explain the spatial localization of the transiently observed pattern.

3.1.1. *Bifurcation branch of skewed varicose states*

When convection patterns in experiments or numerical simulations exhibit complex dynamics, we expect the existence of invariant states underlying the pattern dynamics. For the pattern dynamics emerging from the skewed varicose instability of straight convection rolls R_λ at $\gamma = 0°$ we however do not find invariant states at the control parameters where the dynamics is observed. Direct numerical simulations in a minimal periodic domain can reproduce the transient dynamics of the skewed varicose pattern, but previous analysis of the temporal dynamics did not yield an underlying invariant state (RS19).

An equilibrium state resembling the observed skewed varicose pattern (SV) is identified below ϵ_c of the skewed varicose instability, as described in Section 2.2. Numerical continuation of SV reveals a subcritical ϵ-backward pitchfork bifurcation from $R_{\lambda 2}$ at $\epsilon_c = 1.019$. The bifurcation breaks the continuous translation symmetry $\tau(a_x, 0)$ of straight convection rolls $R_{\lambda 2}$. Here we consider the rolls to be x-aligned and periodic with wavelength λ_y. The bifurcating eigenmode shows a skewed three-dimensional flow structure. The bifurcating equilibrium SV is $[4\lambda_x, 4\lambda_y]$-periodic and invariant under transformations of the symmetry group $S_{sv} = \langle \pi_{xyz}, \tau(0.25, 0.25) \rangle$. From the bifurcation point, the SV-branch continues down in ϵ, undergoes a sequence of folds, and terminates at $\epsilon = 0.206$ in a bifurcation from straight convection rolls $R_{\lambda 3}$ with wavelength $\lambda = 2.8$ (panel $\gamma = 0°$ in Figure 3). Thus, the equilibrium state SV connects two equilibrium states representing straight convection rolls at different wavelengths. SV exists only below the critical threshold parameter ϵ_c. The pure subcritical existence of SV explains why no temporal transition to an underlying invariant state at $\epsilon > \epsilon_c$ has been found in RS19.

Since the bifurcation branches are very cluttered at $\gamma = 0°$ in Figure 3, we reproduce the bifurcation diagram schematically. In Figure 5, the bifurcation branches are plotted in terms of their approximate dominating pattern wavelength λ_p as a function of ϵ. Along the SV-branch, convection rolls develop skewed relative orientations (Figure 5b) until the rolls pinch-off and reconnect at an oblique orientation (Figure 5c). At the bifurcation point, $R_{\lambda 3}$ is rotated by 74.6° against the orientation of $R_{\lambda 2}$ (Figure 5a,c). To link these two different roll orientations, the continuous deformations in the skewed varicose pattern skip two instances for potential reconnection to straight rolls with orientations in between. Each of the potential reconnection points corresponds to a pair of folds along the SV-branch. Here, three pairs of folds are observed but this number is specific to the chosen domain size. In between the first two folds at $0.94 < \epsilon < 0.95$, the SV-branch is bistable with $R_{\lambda 2}$ and $R_{\lambda 3}$ in a symmetry subspace of S_{sv}. The stability of all branches is indicated by the linestyle. Overall, the bifurcation diagram indicates coexistence of stable (or weakly unstable) SV with stable $R_{\lambda 2}$ and $R_{\lambda 3}$ over a range of ϵ. The coexistence of

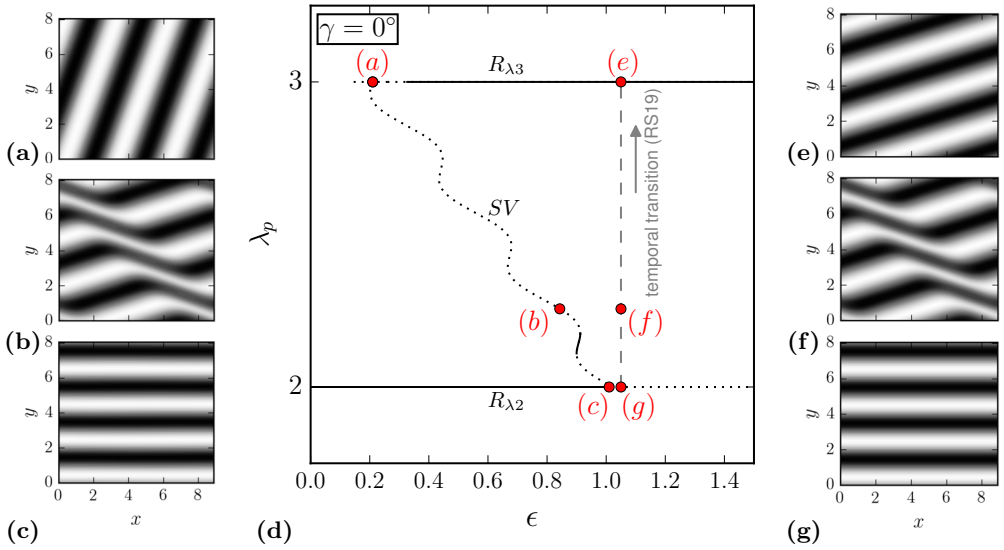

Figure 5: For $\gamma = 0°$ (Rayleigh-Bénard), the subcritical bifurcation of the skewed varicose state (SV) connects two equilibrium states of straight convection rolls at different wavelength and orientation. Midplane temperature fields of equilibrium states **(a-c)** are chosen along the SV-branch, plotted here in a schematic bifurcation diagram in terms of an approximate dominating pattern wavelength λ_p over ϵ in **(d)**. A simulated temporal transition from unstable $R_{\lambda 2}$ to stable $R_{\lambda 3}$ at supercritical $\epsilon > \epsilon_c$ (RS19) is indicated by the dashed line. Snapshots from the temporal transition **(g,f,e)** show matching skewed varicose patterns between the equilibrium state **(b)** for $\epsilon < \epsilon_c$ and the transient state **(f)** at $\epsilon > \epsilon_c$. The orientation of $R_{\lambda 3}$ differs between the terminating bifurcation branch at $\epsilon = 0.2$ **(a)** and the attracted temporal dynamics at $\epsilon = 1.05$ **(e)**.

invariant states suggests spatial coexistence of straight convection rolls and the skewed varicose patterns.

The convection pattern along the SV-branch at $\epsilon < \epsilon_c$ may be compared to the convection pattern observed transiently in time along a simulated transition at $\epsilon = 1.05 > \epsilon_c$ (dashed line in Figure 5d and Section 4.3 in RS19). The midplane temperature contours of SV along its subcritical bifurcation branch partly match the transient patterns along the supercritical temporal transition. We find matching patterns at initial instances in time when straight convection rolls are observed (Figure 5c,g), and at intermediate time when the transient pattern of skewed varicose pattern emerges (Figure 5b,f). Thus, SV indeed captures the observed transient pattern triggered by the skewed varicose instability, but the comparison is for different ϵ. This observation raises the question how the transient temporal dynamics observed above critical thresholds can be related to an equilibrium state existing only below critical thresholds.

3.2. *Subharmonic oscillations - standing and traveling waves*

Subharmonic oscillations are observed as standing wave patterns emerging in spatially localized patches that may travel across extended domains (Daniels *et al.* 2000; Subramanian *et al.* 2016). Here, the periodic orbit SSW, underlying the standing wave, is found to coexist with a traveling wave state. Standing and traveling wave states al-

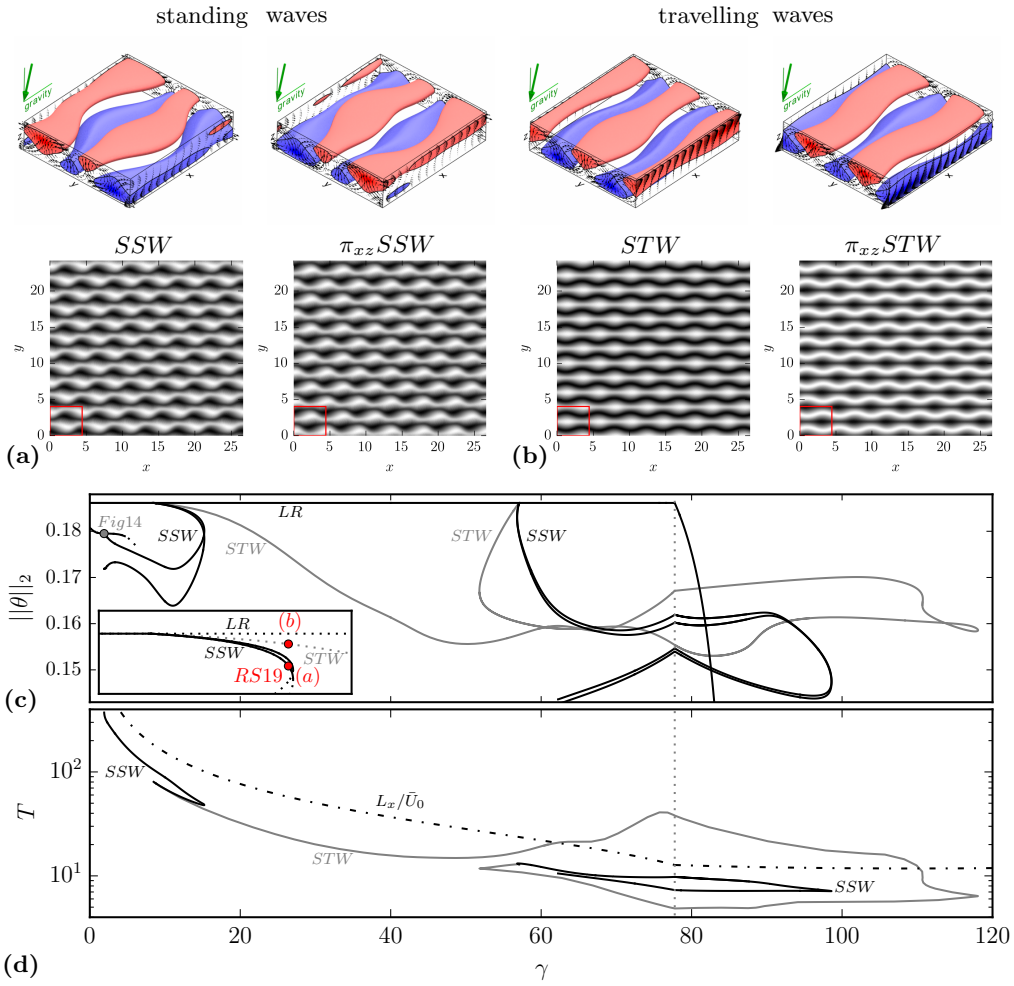

Figure 6: Symmetry-related pairs of standing wave states SSW **(a)** and traveling wave states STW **(b)** bifurcate together in equivariant Hopf-bifurcations from LR. The pattern of SSW and STW is visualised by temperature contours in three and two dimensions (midplane). The bifurcation diagram in **(c)** shows the branches of SSW (black) and STW (grey) at $\epsilon = 1.5$. Other branches shown in Figure 4 for $\epsilon = 1.5$ are suppressed for clarity. The inset indicates stable (solid) and unstable (dotted) branches close to the bifurcation at $\gamma = 8.5°$ giving rise to the states in **(a)** and **(b)** at $\gamma = 15°$. 'RS19' labels the control parameter where temporal dynamics has been studied in RS19. Panel **(d)** illustrates how the orbit period T_{ssw} of SSW and the travel time T_{lsw} of STW across L_x approximately follow the mean advection time $L_x/\bar{U}_0$ of the laminar base flow B (dashed-dotted line). Note the 'hydrolic jumps' where phase and advection velocity match at $\gamma = 65°$ and at $\gamma = 110°$ of the STW-branch.

ways bifurcate together in equivariant Hopf bifurcations. Both, standing and traveling waves capture observed patterns of spatially subharmonic oscillations. The existence of a traveling wave state explains the observed traveling dynamics of the pattern.

3.2.1. *Equivariant Hopf bifurcation from longitudinal rolls*

Starting from the periodic orbit SSW, found at $[\gamma, \epsilon] = [15°, 1.5]$ in RS19, we continue the branch down in γ. The SSW-branch bifurcates from LR at $[\gamma_c, \epsilon_c] = [8.5°, 1.5]$. This bifurcation is a γ-forward, supercritical Hopf bifurcation with a critical orbit period of $T_{\mathrm{ssw}} = 80.2$. The bifurcation corresponds to four complex eigenvalues crossing the imaginary axis at $\omega_i = \pm 0.078$ controlling the period $T_{\mathrm{ssw}} = 2\pi/|\omega_i|$. The Hopf bifurcation to SSW accounts only for one pair of complex neutral eigenmodes. The other pair gives rise to a traveling wave state that we term subharmonic traveling wave (STW) with a critical phase speed of $c = L_x/T_{\mathrm{lsw}} = 0.055$ where $T_{\mathrm{lsw}} = T_{\mathrm{ssw}}$. Both invariant states, the π_y-symmetric STW and the π_{xyz}-symmetric SSW (shown in left panels of Fig. 6(a) and (b)), each have a counter-propagating sibling state obtained via π_{xz}-transformation. Both invariant states capture a subharmonic oscillatory convection pattern invariant under $\tau(0.5, 0.5)$. An equilibrium pattern very close to STW can be observed in spatially forced horizontal convection (Weiss *et al.* 2012). STW also resembles the subharmonic "sinucose" state arising from an instability of longitudinal streaks in pure shear flow (Waleffe 1997).

At parameters where SSW and STW bifurcate locally from LR, they share the same bifurcation point (see panels for $10° \leqslant \gamma \leqslant 60°$ in Figure 3. This robust feature in the bifurcation diagram is a consequence of equivariant Hopf bifurcations. It is known that Hopf bifurcations that break the $O(2)$-symmetry of a flow must result in two branches originating from the bifurcation: A standing wave branch and a traveling wave branch (Knobloch 1986). At most one of the two branches is stable. In the present case, the Hopf bifurcation breaks the $O(2)_x$-symmetry of LR. The bifurcation at $[\gamma_c, \epsilon_c] = [8.5°, 1.5]$ (inset panel in Figure 6c) has both the branches bifurcating supercritically. SSW is initially stable and STW is unstable. This corresponds to one specific of six discussed cases in Knobloch (1986). However, here the bifurcation is secondary. While in Knobloch (1986), bifurcations from a non-patterned two-dimensional primary state with a spatial $O(2)$-symmetry are discussed, here, the bifurcating secondary equilibrium state LR is a three-dimensional state that is symmetric under transformations of $O(2) \times Z_2$. The additional third dimension and the additional reflection symmetry do not affect the conditions necessary for equivariant Hopf bifurcations (Knobloch 1986).

Continuations of SSW and STW in γ reveal their existence over a large range of inclination angles γ, including $\gamma > 90°$ where their parent state LR does not exist anymore (Figure 6c). Over this range in γ, the orbit period of SSW and the propagation time $T_{\mathrm{lsw}} = L_x/c$ of STW with phase velocity c and $L_x = 2\lambda_x$ follow approximately the mean laminar advection time $L_x/\bar{U}_0$ (Figure 6d). While the state branch of STW at $\epsilon = 1.5$, shown as light grey line in Figure 6c, connects two Hopf bifurcations, one at small and one at large γ, the SSW branches at $\epsilon = 1.5$, shown as black lines in Figure 6c, originating from these two bifurcations remain disconnected. The branch bifurcating forward at $\gamma_c = 8.5°$ undergoes a fold at $\gamma = 15.2°$ (Figure 6c) explaining why no temporal state transition from LR to SSW was found at $\gamma = 17°$ in RS19. The fold destabilizes SSW and connects to a state branch reaching to subcritical parameters where LR is linearly stable. Similar folds occur under ϵ-continuations at $\gamma = 10°$ and $\gamma = 20°$. Beyond these folds, SSW state branches terminate and show 'loose ends' in the bifurcation diagrams. These terminations correspond to global bifurcations which we explain in the next subsection.

3.2.2. *Global bifurcation to subharmonic standing waves*

The global bifurcation at $\gamma = 10°$ occurs at $\mathrm{Ra}_c = 2230.25$ ($\epsilon_c = 0.286$) where the pre-periodic orbit SSW, satisfying (2.7) with $\sigma_{\mathrm{ssw}} = \pi_y \tau(0.25, 0.25)$ and a pre-period

of $T' = T/4$, collides with a heteroclinic cycle between two symmetry related saddle states TR and $\sigma_{\mathrm{ssw}}TR$ (Figure 7). At the global bifurcation point, the spectrum of eigenvalues of TR is computed in a symmetry subspace Σ_0 given by the $[2\lambda_x, 2\lambda_y]$-periodic domain with imposed symmetries of SSW, namely $\tau(0.5, 0.5)$ and π_{xyz}. The five leading eigenvalues are real and read $[\omega_1, \omega_2, \omega_3, \omega_4, \omega_5] = [0.048, 0.045, -0.090, -0.120, -0.138]$. The midplane temperature contours of the associated eigenmodes $[\boldsymbol{e}_1^u, \boldsymbol{e}_2^u, \boldsymbol{e}_3^s\boldsymbol{e}_4^s, \boldsymbol{e}_5^s]$ are given in Figure 7h. Eigenvalues and eigenmodes of TR do not change significantly when Ra crosses Ra_c. In contrast to the heteroclinic cycle discussed in RS19, where each of the two symmetry related instances of OWR has a single unstable eigenmode, the present cycle connects symmetry related instances of TR with two unstable eigenmodes each. Perturbations of TR with the eigenmode $\boldsymbol{e}_1^u$ trigger a state transition $TR \to \sigma_{\mathrm{ssw}}TR$ while perturbations with $\boldsymbol{e}_2^u$ lead to LR which is dynamically stable in Σ_0 at these control parameters. The symmetry relation between TR and $\sigma_{\mathrm{ssw}}TR$ guarantees that $\sigma_{\mathrm{ssw}}TR$ has the same eigenvalues as TR and symmetry related eigenmodes $\sigma_{\mathrm{ssw}}[\boldsymbol{e}_1^u, \boldsymbol{e}_2^u, \boldsymbol{e}_3^s, \boldsymbol{e}_4^s, \boldsymbol{e}_5^s]$ allowing for the returning transition $\sigma_{\mathrm{ssw}}TR \to TR$ to close the heteroclinic cycle.

Direct numerical simulations indicate that states close to the heteroclinic cycle are eventually attracted to LR. To show that this heteroclinic cycle is dynamically unstable but structurally stable, we identify two symmetry subspaces of Σ_0 in which either $TR \to \sigma_{\mathrm{ssw}}TR$ or $\sigma_{\mathrm{ssw}}TR \to TR$ exists as heteroclinic connection between an equilibrium with a single unstable eigenmode and a dynamically stable equilibrium. By doing so, the heteroclinic cycle is shown to satisfy all conditions of a structurally stable, or robust, heteroclinic cycle between two symmetry related equilibrium states (Krupa 1997), also discussed in RS19. Subspace Σ_1 is given by imposing the symmetries in the group $\langle \pi_y, \pi_{xz}, \tau(0.5, 0.5)\rangle$ and contains the connection $TR \to \sigma_{\mathrm{ssw}}TR$. Of the five initially considered eigenmodes in Σ_0, TR in Σ_1 has still $[\boldsymbol{e}_1^u, \boldsymbol{e}_3^s, \boldsymbol{e}_5^s]$ and $\sigma_{\mathrm{ssw}}TR$ in Σ_1 has still $\sigma_{\mathrm{ssw}}[\boldsymbol{e}_4^s, \boldsymbol{e}_5^s]$. Subspace Σ_τ is given by imposing the symmetries in the group $\langle \pi_y\tau(0.5, 0), \pi_{xz}\tau(0.5, 0), \tau(0.5, 0.5)\rangle$ and contains the connection $\sigma_{\mathrm{ssw}}TR \to TR$. Of the five initially considered eigenmodes in Σ_0, $\sigma_{\mathrm{ssw}}TR$ in Σ_τ has still $\sigma_{\mathrm{ssw}}[\boldsymbol{e}_1^u, \boldsymbol{e}_3^s, \boldsymbol{e}_5^s]$ and TR in Σ_τ has still $[\boldsymbol{e}_4^s, \boldsymbol{e}_5^s]$. Using the classification of eigenvalues and associated stability theorem in Krupa & Melbourne (1995), we identify ω_1 as expanding, ω_2 as transverse, ω_4 as contracting and ω_5 as radial eigenvalue. Eigenvalue ω_3 exists in the same subspace as the expanding eigenvalue ω_1 and therefore does not affect the dynamical stability. Since $\min(-\omega_4, \omega_1 - \omega_2) \not> \omega_1$, the heteroclinic cycle is not asymptotically stable (Krupa & Melbourne 1995, Theorem 2.7).

Before SSW disappears in the global bifurcation at Ra_c, the solution branch undergoes a fold at $\mathrm{Ra} < \mathrm{Ra}_c$ (Figure 8a). The existence of such a fold near a global bifurcation follows from the dynamical stability of the bifurcating periodic orbit relative to the dynamical stability of the heteroclinic cycle. To analyse the stability, we consider the linearised dynamics around the heteroclinic cycle $TR \to \sigma_{\mathrm{ssw}}TR \to TR$ at Ra_c and obtain the following Poincaré map (see Bergeon & Knobloch 2002, for a derivation)

$$\zeta_{i+1} = c\zeta_i^\rho + \mu, \quad \rho = -\frac{\omega_4}{\omega_1} = 2.51 \ , \tag{3.7}$$

with constant $c > 0$ and control parameter $\mu \propto \mathrm{Ra}_c - \mathrm{Ra}$. Variable $\zeta_i \ll 1$ describes a local coordinate in a Poincaré section located at a distance $\varepsilon \ll 1$ from TR and defining a small perturbation around the state vector of TR as $\boldsymbol{x}' = \boldsymbol{x}_{TR} + \zeta_i\boldsymbol{e}_1^u + \varepsilon\boldsymbol{e}_4^s$. The heteroclinic cycle corresponds to $\zeta_i = 0$ and is reached at $\mu = 0$. The bifurcating periodic orbit is a fixed point $\bar{\zeta}$ of the map such that $\bar{\zeta} = c\bar{\zeta}^\rho + \mu$. Since $\rho > 1$, a nearby fixed point $\bar{\zeta}$ exists only for $\mu > 0$ and $\mathrm{Ra} < \mathrm{Ra}_c$, respectively. The graph in Figure 8b illustrates the map (3.7) and shows that the fixed point $\bar{\zeta}$ is dynamically stable.

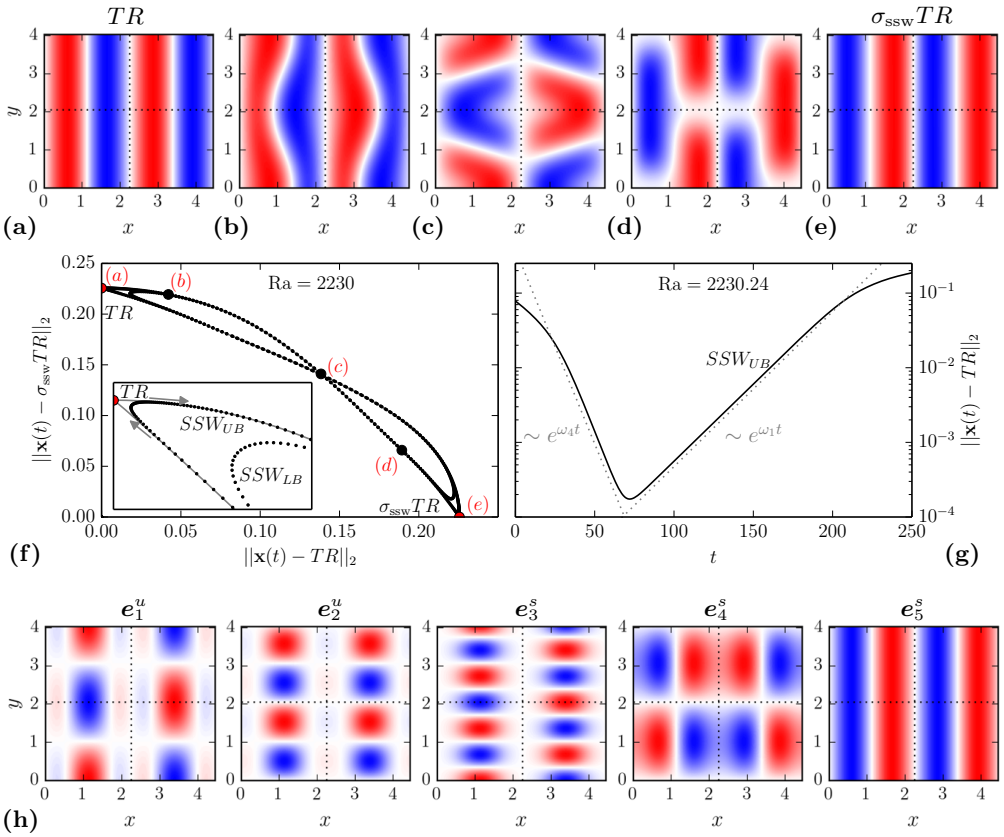

Figure 7: The pre-periodic orbit SSW approaches a global bifurcation at $\gamma = 10°$ and $\mathrm{Ra}_c = 2230.25$ ($\epsilon_c = 0.286$) where it collides with a robust heteroclinic cyle between TR and the symmetry related equilibrium $\sigma_{ssw}TR$ with $\sigma_{\mathrm{ssw}} = \pi_y\tau(0.25, 0.25)$. **(a-e)** Sequence of midplane temperature contours along the dynamical connection $TR \to \sigma_{ssw}TR$ at $\mathrm{Ra} = 2230$. **(f)** State space projection of the lower (LB) and the upper branch (UB) of SSW (cf. Figure 8a). Inset enlarges the orbit trajectories (black dots) near TR and the heteroclinic cycle (grey lines). **(g)** L_2-distance of the SSW_{UB} orbit trajectory from TR at $\mathrm{Ra} = 2230.24$ very close to Ra_c. The dynamics of SSW_{UB} is exponential for most of the pre-period and governed by two eigenvalues of TR. **(h)** Midplane temperature contours of two unstable and three stable eigenmodes $\boldsymbol{e}_i^{u/s}$ of TR associated to the five leading eigenvalues $[\omega_1, \omega_2, \omega_3, \omega_4, \omega_5] = [0.048, 0.045, -0.090, -0.120, -0.138]$ of TR.

The stability of $\bar{\zeta}$ assumes that no additional transverse eigendirections are unstable. However, the symmetry subspace that contains SSW also contains $\boldsymbol{e}_2^u$ which must be taken into account. Thus, the above analysis predicts that SSW bifurcates with a single unstable eigendirection from the heteroclinic cyle, namely $\boldsymbol{e}_2^u$. Since SSW for $\mathrm{Ra} > \mathrm{Ra}_c$ has two unstable eigenmodes, the periodic orbit must undergo a fold prior to the global bifurcation to stabilise the extra unstable eigendirection. Such a fold also exists at $\gamma = 20°$ (Figure 3) but further away from the global bifurcation. Note that unlike the global bifurcation discussed in Bergeon & Knobloch (2002), the present bifurcation involves first, a heteroclinic cycle between two symmetry related equilibrium states and second, a dynamically unstable periodic orbit such that the fold may have a stabilising effect.

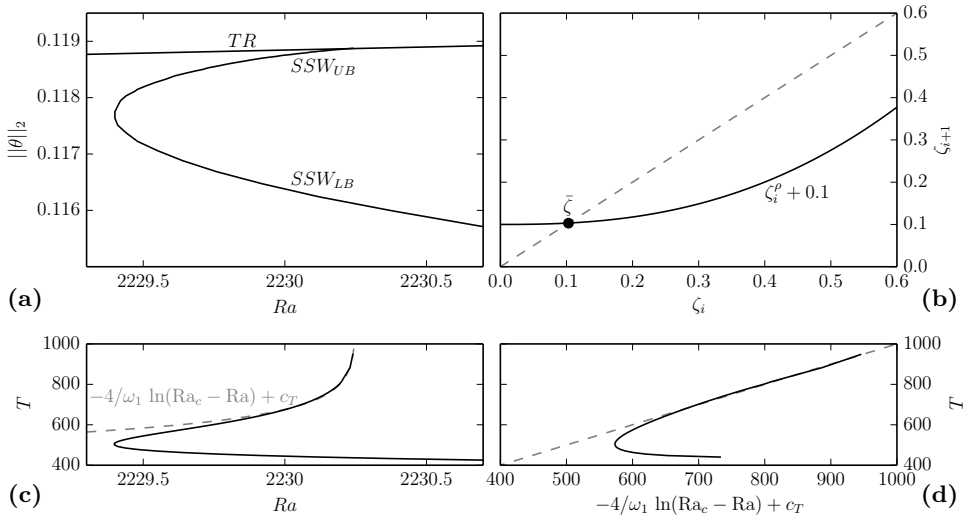

Figure 8: Before SSW disappears in a global heteroclinic bifurcation at $\gamma = 10°$ and $\mathrm{Ra}_c = 2230.25$ ($\epsilon_c = 0.286$), the branch undergoes a saddle node bifurcation. **(a)** Enlarged bifurcation diagram showing the branch of SSW indicating the maximum $||\theta||_2$ over one cycle (cf. panel $\gamma = 10°$ in Figure 3). **(b)** Graphical representation of the linearised Poincaré map (3.7) for $\mu = 0.1$ around the heteroclinic cycle between symmetry related instances of TR. The fixed point $\bar{\zeta}$ is stable as the slope of the map at $\bar{\zeta}$ is less than one (dashed line). **(c,d)** Towards the global bifurcation, the orbit period of SSW approaches an infinite period according to a logarithmic scaling law shown as a function of Ra in **(c)** and for rescaled Ra in **(d)**. This law follows from the linearised map (3.7). Here, the constant is $c_T = 560$.

The period of SSW must increases towards an infinite time period as the periodic orbit approaches the heteroclinic cycle. The map (3.7) suggests a scaling law for $T \sim \mathrm{Ra}$ close to the global bifurcation. Since $\zeta \ll 1$ and $\rho > 1$, the periodic orbit is given by the approximation $\bar{\zeta} \approx \mu$. Over a full period of SSW, the orbit trajectory visits both TR and $\sigma_{\mathrm{ssw}}TR$ twice. The time the orbit trajectory spends in the ε-neighborhood of TR or $\sigma_{\mathrm{ssw}}TR$ dominates the entire orbit period T (Figure 7g) such that T satisfies the approximation $\bar{\zeta} \approx \varepsilon \exp(-\omega_1 T/4)$. Hence, the period of SSW is expected to increase with $T \sim -4/\omega_1 \ln(\mathrm{Ra}_c - \mathrm{Ra})$. Using a mutli-shooting method, SSW is continued close to the global bifurcation. The increasing orbit period confirms the predicted scaling law (Figure 8c,d).

3.3. *Wavy rolls with defects - connecting coexisting state branches*

Convection patterns of wavy rolls are observed to quickly incorporate defects in large experimental domains (Daniels & Bodenschatz 2002; Daniels *et al.* 2008). These defects may form interfaces between spatially coexisting wavy rolls at different orientations against the base flow. Here, a bifurcation and stability analysis of WR reveals four new equilibrium states, including obliquely oriented states and rolls with defects, that all coexist with WR for the same control parameters. The multiple states can give rise to the observed spatial coexistence.

3.3.1. *Pitchfork bifurcations from longitudinal rolls*

Equilibrium states WR emerge either in pitchfork bifurcations from LR at inclinations $20^\circ \leqslant \gamma \leqslant 80^\circ$ or in saddle-node bifurcations in the absence of LR at $90^\circ \leqslant \gamma \leqslant 100^\circ$. The fact that WR can exist without bifurcating from LR is known from thermal Couette flow (Clever & Busse 1992). Almost all computed pitchfork bifurcations from LR to WR are either ϵ-forward or γ-backward. This observation holds even when the WR-branches develop additional folds, like in the bifurcation diagrams at $\gamma = 80^\circ$ or at $\epsilon = 1.5$. The only γ-forward bifurcation of WR from LR is observed at $\epsilon = 0.1$ (Figure 4, $\epsilon = 0.1$).

3.3.2. *Additional bifurcations from wavy rolls*

In most cases, WR-branches continue to large ϵ. This does not imply the absence of connections to other invariant states. When WR lose stability, additional bifurcations occur. We demonstrate the increasing number of invariant states and their patterns by following the higher order instabilities of WR at $\gamma = 40^\circ$. Arnoldi iteration for WR indicates the stability of the WR-branch up to $\epsilon = 0.256$ in a $[2\lambda_x, \lambda_y]$-periodic domain (Figure 9f). At this point, a subcritical pitchfork bifurcation breaks the π_{xz}- and π_y-symmetry and gives rise to an equilibrium state showing disconnected wavy rolls and named DWR. DWR is invariant under π_{xyz}. Following the DWR-branch from the pitchfork bifurcation, it undergoes a saddle-node bifurcation at $\epsilon = 0.254$, becomes bistable with WR and connects to an equilibrium state of oblique rolls (OR) that continues as a stable branch to larger values of ϵ. DWR represents stationary roll defects that along its branch breaks the topology of rolls in a double periodic domain (Figure 9b), and connects convection rolls at different orientations.

OR is a secondary state bifurcating from the laminar flow B. The oblique orientation at angle $\tan^{-1}(\lambda_y/2\lambda_x)$ against the laminar flow direction coincides with the diagonal of the $[2\lambda_x, \lambda_y]$-periodic domain (Figure 9c). OR is invariant under transformations of $S_{\mathrm{or}} = \langle \pi_{xyz}, \tau(a_x, \pm a_x) \rangle$ corresponding to an $O(2)$-symmetric state. The sign of continuous shift factor a_x differs between left ($+$) and right ($-$) oblique rolls, with $OR^l = \pi_y OR^r$. When OR becomes unstable, an ϵ-forward pitchfork bifurcation at $\epsilon = 0.456$ gives rise to stable oblique wavy rolls (OWR), see Figure 9d. As OR, OWR can have left or right orientation. The symmetry group of OWR is $S_{\mathrm{owr}} = \langle \pi_{xyz}, \tau(0.5, \pm 0.5) \rangle$. Equilibrium OWR with a wavy pattern of wavenumber $m = 2$ along the domain diagonal loses stability at $\epsilon = 0.463$ to an equilibrium OWR_1 with a pattern wavenumber of $m = 1$ and broken $\tau(0.5, \pm 0.5)$-symmetry. The branch of OWR_1 undergoes a saddle-node bifurcation at $\epsilon = 0.477$ and terminates on OR at $\epsilon = 0.476$ (Figure 9f). The small ϵ-range with $\Delta\epsilon = 0.476 - 0.456 = 0.02$ between the two symmetry-breaking bifurcations of OWR_1 with $m = 1$ and OWR with $m = 2$ from OR suggests a nearby codimension-2 point with spatial 1:2 resonance. When stable OWR_1 disappear in the saddle-node bifurcation, the temporal dynamics becomes attracted to a robust heteroclinic cycle between unstable instances of OWR that is discussed in RS19. The branch of OWR continues as unstable branch until it terminates at $\epsilon = 0.8$ on ribbons (RB), an unstable equilibrium state bifurcating together with OR from B in an equivariant pitchfork bifurcation (Figure 9e). The detailed properties of RB are discussed in the following section, but we already note that RB shows disconnected rolls or plumes, similar to DWR. Thus, we find two instances of bifurcation sequences that may be described as "straight rolls bifurcate to wavy rolls, wavy rolls bifurcate to disconnected rolls". In one instance the sequence happens for longitudinal orientation and in the other instance for oblique orientation. The fact that all of the above states coexist with the WR branch at equal control parameters explains that all patterns represented by the invariant states can spatially coexist with wavy rolls in large domains.

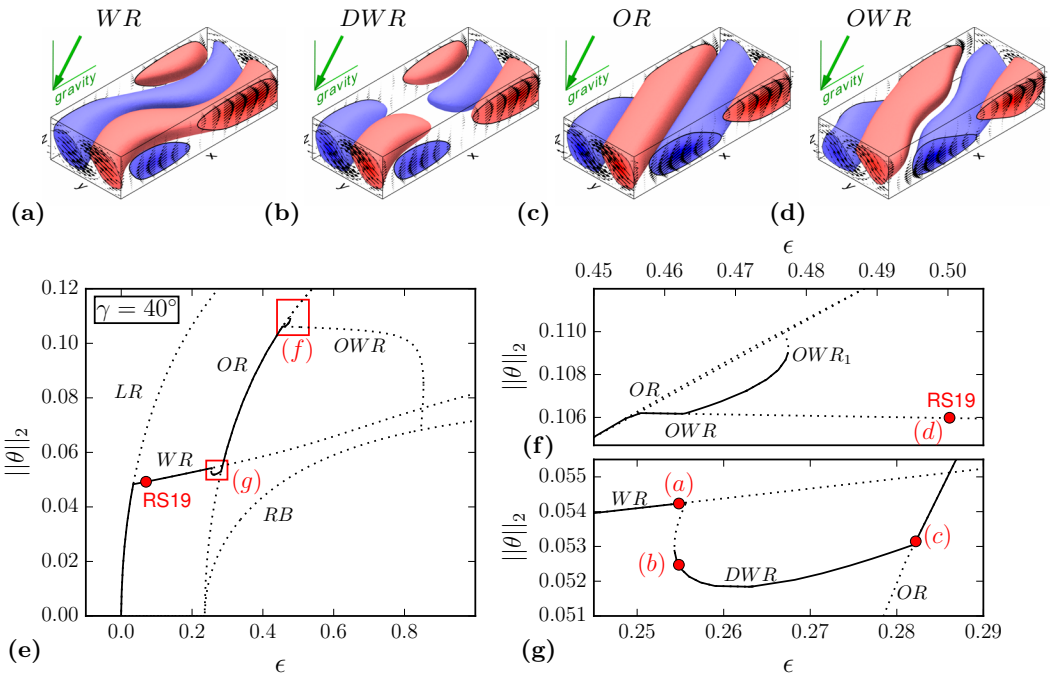

Figure 9: Bifurcation sequence from wavy rolls to oblique wavy rolls **(a-d)**. Bifurcation diagram **(e)** shows how seven equilibrium states are connected over ϵ and indicates stable (solid) and unstable (dotted) parts of the branches. Dynamical stability is computed by Arnoldi iteration in a $(2\lambda_x, \lambda_y)$-periodic domain. Panel **(g)** enlarges the parameter region where DWR connects WR with OR. Panel **(f)** enlarges the parameter region where OWR_1 with pattern wavenumber $m = 1$ connects OWR with pattern wavenumber $m = 2$ with OR. 'RS19' labels the control parameter values at which temporal dynamics have been studied in RS19.

3.4. *Knots and ribbons - two different types of bimodal states*

Observations of knot patterns exist in horizontal convection (Busse & Whitehead 1974; Busse & Clever 1979) and inclined layer convection (Daniels *et al.* 2000). They have been described as 'bimodal convection' in both cases. Here, the properties of equilibrium states for knots are compared to ribbons, a bimodal state identified in the previous section. A decomposition along their bifurcation branches implies that knots and ribbons are bimodal states that fundamentally differ in their bifurcation structure.

3.4.1. *Bifurcations to states for knots and ribbons*

KN at $\gamma = 80°$ bifurcates ϵ-forward from TR. At smaller $||\theta||_2$ than TR, KN continues without folds and terminates in ϵ-backward bifurcations from LR (Figure 3, $\gamma = 80°$). This bifurcation sequence requires $\gamma > \gamma_{c2}$ and was previously analysed using two-mode interactions (Fujimura & Kelly 1993). At $\gamma = 90°$, LR does not exist at finite ϵ and the KN-branch terminates in a bifurcation from an equilibrium state we term subharmonic lambda plumes (SL) and briefly discuss in Appendix A.

RB is an equilibrium state found via continuing the state branches of OWR and WR that terminate in ϵ-bifurcations from RB at $\gamma = 40°$ and $\gamma = 50°$, respectively (Figure 3). RB is invariant under transformations of $S_{\mathrm{rb}} = \langle \pi_y, \pi_{xz}, \tau(0.5, 0.5) \rangle$. Neither

experiments nor simulations of ILC observe the pattern of RB as dynamically stable pattern at the considered parameters. However, we refer to experimental observations of "ribbons" in Taylor-Couette flow (Tagg *et al.* 1989). Ribbons in Taylor-Couette flow are analogous to ribbons in ILC. In Taylor-Couette flow, they bifurcate together with oblique spirals (Chossat & Iooss 1994) and are connected via oblique wavy cross-spirals (Pinter *et al.* 2006), two states that are comparable to OR and OWR in ILC. As in the Taylor-Couette flow, OR and RB in ILC bifurcate robustly together in equivariant bifurcations (Knobloch 1986) and are connected via OWR. However, OR and RB are stationary states and their bifurcation is an equivariant pitchfork bifurcation, unlike equivariant Hopf bifurcations such as those found in Taylor-Couette flow, and those discussed in Section 3.2.

3.4.2. *Decomposition in terms of straight convection rolls*

As a consequence of the stationary equivariant bifurcation, the linear relation $\boldsymbol{x}_{RB} = \alpha\,\boldsymbol{x}^l_{OR} + \beta\,\boldsymbol{x}^r_{OR}$ with $\alpha = \beta$ holds at the bifurcation points, where $\boldsymbol{x}_{RB}$ indicates the state space vector of RB, and $\boldsymbol{x}^l_{OR}$ and $\boldsymbol{x}^r_{OR}$ are the state space vectors of OR^l and OR^r, respectively. This linear decomposition is valid for all parameters, where RB and OR bifurcate from laminar flow B. Since RB emerges as linear superposition of two differently oriented straight convection rolls, we call RB a 'bimodal state'. The term 'bimodal' has been used previously to describe knot patterns of straight convection rolls at orthogonal orientations in experiments of Rayleigh-Bénard convection (Busse & Whitehead 1974) and in experiments of ILC for $\gamma > \gamma_{c2}$ (Daniels *et al.* 2000). In line with previously used terminology, we describe KN and RB both as bimodal states. However, there are fundamental differences between KN and RB bimodal states that are illustrated by the subsequently discussed decomposition analysis.

We consider a bimodal equilibrium state vector $\mathbf{b}(\epsilon)$ depending on continuation parameter ϵ as decomposition

$$\mathbf{b}(\epsilon) = \alpha(\epsilon)\,\mathbf{m}_1(\epsilon) + \beta(\epsilon)\,\mathbf{m}_2(\epsilon) + \mathbf{d}(\epsilon) \tag{3.8}$$

where $\alpha, \beta \in \mathbb{R}$ and $\mathbf{m}_1, \mathbf{m}_2$ are state vectors of two differently oriented straight convection rolls. $\mathbf{d}$ is the difference vector that is necessary to create the composite state $\mathbf{b}$. We simplify the notation by suppressing the dependence of the decomposition on ϵ. We seek the optimal bimodal decomposition (3.8)

$$\langle \alpha\mathbf{m}_1 + \beta\mathbf{m}_2, \mathbf{d}\rangle = 0, \tag{3.9}$$

with $||\mathbf{d}||_2$ minimal. The minimal $\mathbf{d}$ measures nonlinear and non-bimodal effects. The corresponding optimal coefficients α and β may be found via the inner product of (3.8) with $\mathbf{m_1}$ and $\mathbf{m_2}$, respectively,

$$\alpha = \frac{\langle \mathbf{m}_1, \mathbf{b}\rangle}{\langle \mathbf{m}_1, \mathbf{m}_1\rangle} - \beta\frac{\langle \mathbf{m}_1, \mathbf{m}_2\rangle}{\langle \mathbf{m}_1, \mathbf{m}_1\rangle}, \quad \beta = \frac{\langle \mathbf{m}_2, \mathbf{b}\rangle}{\langle \mathbf{m}_2, \mathbf{m}_2\rangle} - \alpha\frac{\langle \mathbf{m}_2, \mathbf{m}_1\rangle}{\langle \mathbf{m}_2, \mathbf{m}_2\rangle}, \tag{3.10}$$

where we assume $\langle \mathbf{m}_1, \mathbf{d}\rangle = 0$ and $\langle \mathbf{m}_2, \mathbf{d}\rangle = 0$ to satisfy (3.9). The inner product $\langle , \rangle$ is induced by the full norm (2.11). (3.10) with (3.8) is a coupled system of equations for the optimal coefficients α and β that we solve iteratively.

The optimal bimodal decomposition (3.8) with (3.10) is calculated for $\mathbf{b} = \boldsymbol{x}_{RB}$ and $\mathbf{m}_{1,2} = \boldsymbol{x}^{l,r}_{OR}$ along the ϵ-bifurcation branches at $\gamma = 40°$. The coefficients are found to be equal at all ϵ, and to decrease linearly from $\alpha = \beta = 0.3291$ at the bifurcation point (Figure 10). The difference vector $\mathbf{d}$ increases linearly in $||\theta||_2$ and mostly accounts for corrections to the flow at the streamwise interfaces between hot and cold plumes (Figure 10d).

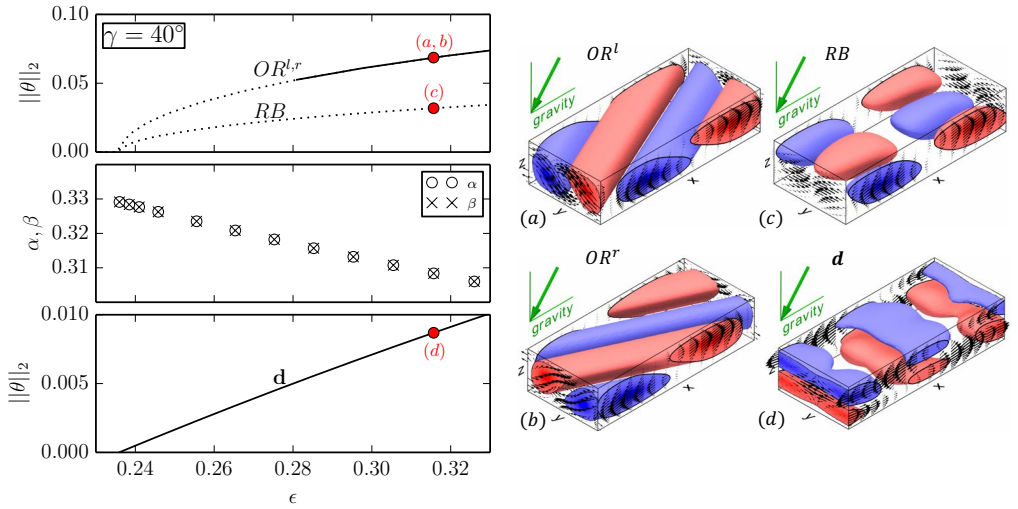

Figure 10: Decomposition of bimodal ribbons (RB) into left and right oriented oblique rolls ($OR^{l,r}$). The bifurcation diagram with details of the decomposition (left) is shown together with visualisations of the temperature and velocity fields on the right (red labels in the diagram indicate panels on the right). RB bifurcates together with $OR^{l,r}$ in equivariant pitchfork bifurcations from the laminar base flow. At $\gamma = 40°$, RB emerges with one additional unstable eigendirection, and $OR^{l,r}$ become dynamically stable in a $[2\lambda_x, \lambda_y]$-periodic domain at $\epsilon = 0.282$ (solid line in top left panel). The optimal decomposition $\boldsymbol{x}_{RB}(\epsilon) = \alpha(\epsilon)\,\boldsymbol{x}^l_{OR}(\epsilon) + \beta(\epsilon)\,\boldsymbol{x}^r_{OR}(\epsilon) + \mathbf{d}(\epsilon)$ implies linearly decreasing equal coefficients $\alpha = \beta$ along the branches (middle panel). The difference vector $\mathbf{d}$ grows linearly in $||\theta||_2$ from zero at the bifurcation point (bottom panel). Thus, RB can be viewed as a bimodal state combining two equally contributing oblique rolls.

The optimal bimodal decomposition (3.8) with (3.10) is calculated again for $\mathbf{b} = \boldsymbol{x}_{KN}$ along the KN-branch at $\gamma = 80°$. Since LR does not coexist with most of the KN-branch (Figure 11), the state vectors $\boldsymbol{m}_1 = \boldsymbol{x}_{TR}$ and $\boldsymbol{m}_2 = \boldsymbol{x}_{LR}$ in the decomposition are not considered as ϵ-dependent. We choose the decomposition $\boldsymbol{x}_{KN}(\epsilon) = \alpha(\epsilon)\boldsymbol{x}_{TR}(\epsilon = 0.024) + \beta(\epsilon)\boldsymbol{x}_{LR}(\epsilon = 0.22) + \boldsymbol{d}(\epsilon)$. Here, ϵ parametrises linear interpolation between two bifurcation points. The resulting optimal coefficients α and β in general differ. While the contribution of the longitudinal rolls monotonically increases, the contribution of the transverse rolls decreases (Figure 11). A decomposition with $\alpha = \beta$ is found at $\epsilon = 0.095$, approximately half-way between the bifurcation points and close to the maximum of $||\mathbf{d}||_2$. Note that $\mathbf{d}$ at the maximum amplitude resembles a ribbon pattern (Figure 11d). Towards the bifurcation points, $\mathbf{d}$ decreases parabolically to zero. Since $\mathbf{d}$ combines nonlinear and non-bimodal effects, as well as effects due to interpolation between TR and LR at fixed values of ϵ, the dominant source for the large values of $\partial||\boldsymbol{d}||_2/\partial\epsilon$ at the bifurcations is unclear. Stability analysis of the knot instability indicates a three-mode interaction(Fujimura & Kelly 1993; Subramanian *et al.* 2016), suggesting that a third state is involved as evidenced by the significant contribution of $\boldsymbol{d}$.

KN and RB differ in their bifurcation structure. KN is a connecting state between TR and LR, while RB bifurcates together with $OR^{l,r}$ in an equivariant pitchfork bifurcation. As a consequence, their bimodal decomposition into two composing straight convection rolls differs significantly. RB is composed of an equal weight superposition of two sym-

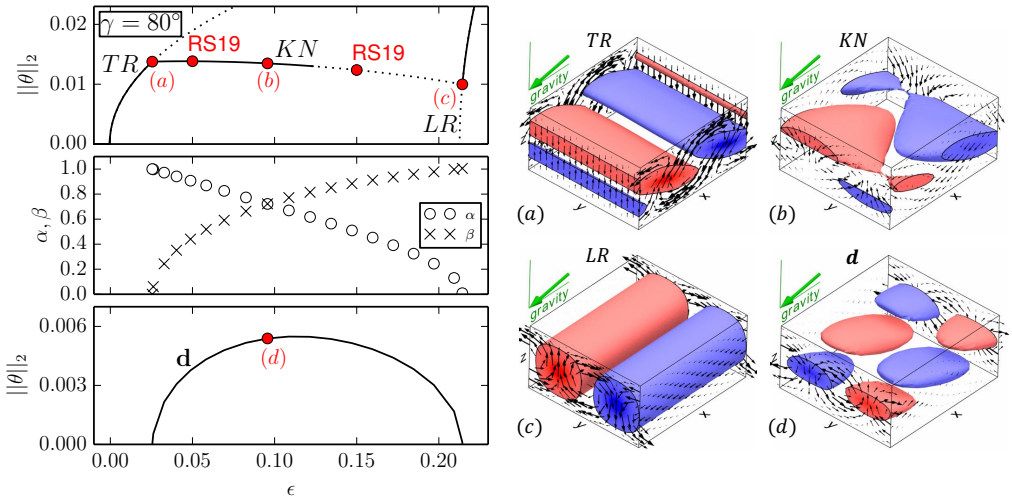

Figure 11: Decomposition of knots (KN) into longitudinal and transverse oriented rolls, LR and TR, respectively. The bifurcation diagram with details of the decomposition (left) is shown together with visualisations of the temperature and velocity fields on the right (red labels in the diagram indicate panels on the right). KN connect TR and LR at $\gamma = 80°$ (top). Dynamical stability in a $[\lambda_x, \lambda_y]$-periodic domain is indicated by the solid lines. 'RS19' labels the control parameter where temporal dynamics has been studied in RS19. Between the bifurcation points, the optimal decomposition $KN(\epsilon) = \alpha(\epsilon)\, TR(\epsilon = 0.024) + \beta(\epsilon)\, LR(\epsilon = 0.22) + \mathbf{d}(\epsilon)$ results in decreasing α, increasing β (middle), and parabolically varying $\mathbf{d}$ (bottom). Thus, KN can be viewed as a bimodal state combining transverse and longitudinal rolls with monotonically changing relative contributions.

metry related oblique rolls $OR^l = \pi_y OR^r$. KN in ILC at $\gamma \neq 0°$ is a mixed mode state, composed of transverse and longitudinal rolls that are not symmetry related and whose weight continuously changes along the branch. At $\gamma = 0°$ however, TR and LR become symmetry related via rotation. The knot patterns observed in Rayleigh-Benard convection (Busse & Whitehead 1974) are thus expected to bifurcate in equivariant pitchfork bifurcations, like RB in ILC .

3.5. *Transverse oscillations - continuation towards a chaotic state space*

The pattern of obliquely modulated transverse rolls, called 'switching diamond panes', shows complex dynamics with chaotically switching pattern orientations (Daniels *et al.* 2000). A periodic orbit TO underlying transverse oscillations has been identified in RS19 at moderate ϵ. The pattern of transverse oscillations seems to capture some aspects of the observed complex dynamics. ϵ-continuations of TO show that the orbit period of TO is subject to large and non-monotonic changes, and the number of unstable eigendirections of TO increases quickly with ϵ. This suggests the existence of complex state space structures that support the chaotic dynamics of switching diamond panes.

3.5.1. *Bifurcations to transverse oscillations*

In all but one analysed parameter continuations, the pre-periodic orbit TO bifurcates from TR in a supercritical Hopf bifurcation. The bifurcations are either ϵ-forward at

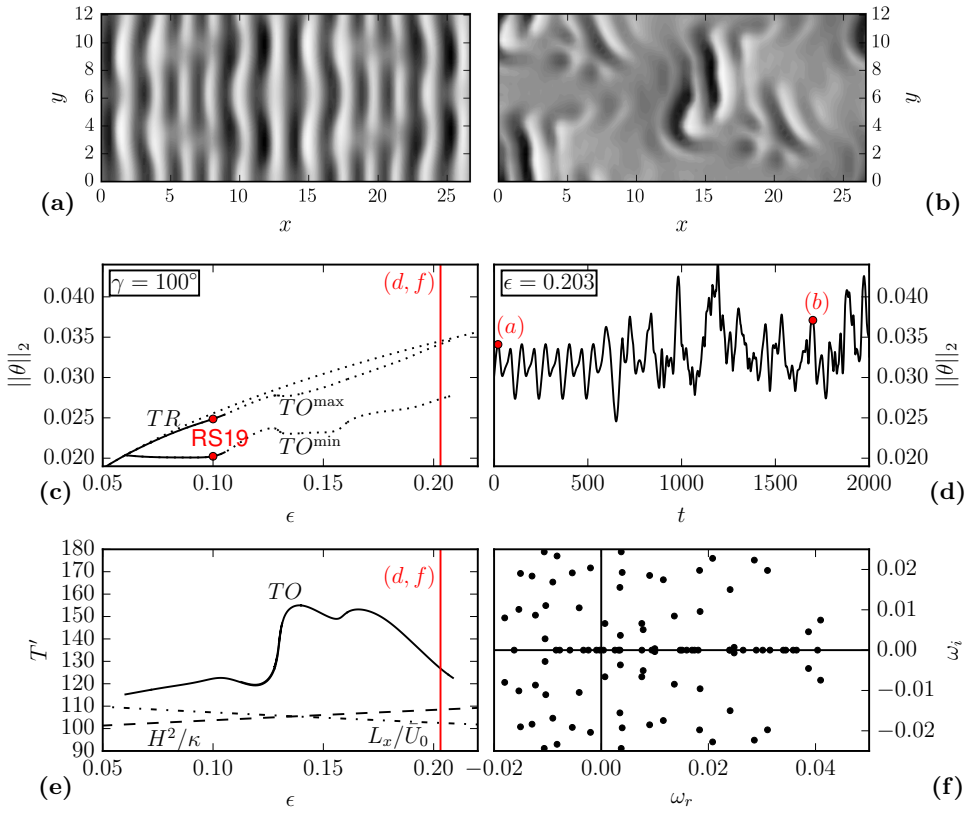

Figure 12: Continuation of TO at $\gamma = 100°$ towards a chaotic state space. **(a)** Midplane temperature of TO at Ra = 11 000 ($\epsilon = 0.203$) before instabilities create a turbulent flow **(b)**. The corresponding simulated time series of TO **(d)** shows the transition from a periodic to a turbulent signal. The transition is a consequence of the many linear instabilities of TO **(f)** that have emerged along the bifurcation branch **(c)**. Solid/dotted bifurcation branches indicate stable and unstable states in the symmetry subspace of $S = \langle \pi_y, \pi_{xz}, \tau(0.5, 0.5) \rangle$. 'RS19' labels the control parameter value at which temporal dynamics has been studied in RS19. The changing relative period T' of TO along the bifurcation branch is shown in **(e)** and compared to the time scale of thermal diffusion H^2/κ and laminar mean advection $L_x/\bar{U}_0$ (dashed and dashed-dotted lines).

$\epsilon \approx 0.07$, found at inclination angles $\gamma = [80°, 90°, 100°, 110°]$, or γ-backward, found at $\epsilon = 0.1$ and $\gamma = 132.2°$. The latter case represents the upper inclination limit of existence of TO at $\epsilon = 0.1$. At the lower limit, just below γ_{c2}, TO bifurcates as quaternary state from the transverse subharmonic varicose state TSV (see inset panel in Figure 4). TSV is an equilibrium state discussed briefly in Appendix A. A common feature of all TO-branches is that the $||\theta||_2$-maximum over the orbit period remains close to the $||\theta||_2$-value of TR. This agrees with the observation that TO modulations are sinusoidal oscillations around strictly transverse rolls with the maximum deflection associated to the minimum in $||\theta||_2$ over the orbit period (RS19).

3.5.2. *Numerical continuation of transverse oscillations*

γ-continuation of TO at $\epsilon = 0.1$ is numerically straight forward and yields periodic orbits showing weak bending modulations around a purely transverse orientation (RS19, Section 4.2.2). ϵ-continuations are found to be numerically challenging for increasing ϵ. We could not continue TO much beyond $\epsilon = 0.2$ (Figure 12c). The reason for the computational difficulty is two-fold. First, the time period of the orbit drastically changes with ϵ, which causes challenges for our shooting method. The pre-periodic orbit TO satisfying (2.7) with $\sigma = \tau(0.5, 0)$ oscillates slowly with a relative period $T' \sim \mathcal{O}(10^2)$ close to the heat diffusion time H^2/κ and the laminar mean advection time $L_x/\bar{U}_0$. Along the continuation, the large orbit period is subject to significant and non-monotonic changes over small ϵ-intervals (Figure 12e). These changes in the orbit period are numerically difficult to trace. Secondly, the iterative solver of the Newton algorithm converges better if the target state is dynamically stable or weakly unstable (Sanchez *et al.* 2004). Computing the spectrum of eigenvalues of TO in the symmetry subspace of $[12\lambda_x, 6\lambda_y]$-periodicity indicates that the state branch at $\gamma = 100°$ and $\epsilon = 0.203$ has collected 63 unstable eigenvalues with a broad range of frequencies ω_i (Figure 12f). At these parameters, the single-shooting Newton algorithm converged TO to a residual of $||\mathcal{G}(\mathbf{x})||_2 < 3 \times 10^{-11}$ (see Equation 2.7). When integrating the converged orbit forward in time, unstable directions trigger a transition to a turbulent state after $t = 500$ (Figure 12d). This turbulent state has been described as longitudinal bursts within switching diamond panes (Daniels *et al.* 2000). We conclude that continuation of TO for $\epsilon > 0.2$ is challenging due to the numerical condition of a temporally slow, spatially large and very unstable periodic orbit that competes with many fast and small-scale modes in a chaotic turbulent state space.

4. Discussion

Towards understanding how temporal and spatio-temporally complex dynamics arises in ILC, we have computed three-dimensional invariant states underlying several observed spatially periodic convection patterns in ILC at Pr = 1.07. Numerical continuation of these invariant states in two control parameters, the normalised Rayleigh number ϵ and the inclination angle γ, yields 15 bifurcation diagrams covering systematically selected parameter sections in the intervals $\epsilon \in [0, 2]$ and $\gamma \in [0, 120)$. For some selected bifurcating state branches, we have characterised their stability properties and pattern features along the branches. These state branches were selected for a more detailed discussion in the present article for two reasons. First, each selected branch bifurcates at a different secondary instability. Second, they cover the control parameters at which the temporal dynamics along dynamical connections between stable and unstable invariant states have previously been described (RS19).

The relevance of the computed invariant states for observed spatio-temporally complex dynamics in ILC depends in general on the type of bifurcation creating the states, the range in control parameters over which state branches exist, and the stability properties of the invariant states along their branches. The dynamical relevance of invariant states in the context of the entire bifurcation structure is discussed below by answering the three specific questions posed in the introduction ($Q1$-$Q3$). To describe the role of individual invariant states for temporal pattern dynamics, we can distinguish three different cases:

In case 1, a stable invariant state represents a dynamical attractor at specific control parameters. This case corresponds for example to supercritical ϵ-forward bifurcations where the stable bifurcating invariant state is an attractor for the dynamics above the criti-

cal control parameters for the bifurcation. For invariant states that have been identified because they represent dynamical attractors at specific control parameters (RS19), the present bifurcation analysis indeed confirms supercritical ϵ-forward bifurcations (Sections 3.2-3.5).

In case 2, invariant states exist at specific control parameters but are dynamically unstable. State branches are only stable over a finite range in control parameters. This range is limited by instabilities along state branches. Invariant states which the present study indicates as dynamically unstable at specific control parameters, may still be relevant for the observed temporal dynamics at these control parameters. One reason is that the range of stability along state branches depends on the considered pattern wavelength. Thus, invariant states might be dynamically stable at other pattern wavelengths not considered here. Another reason is that weakly unstable invariant states may be building blocks for the dynamics supported by a more complex state space attractor. Here, the evolving state vector may transiently visit weakly unstable invariant states by approaching and escaping along their stable and unstable manifolds, respectively (e.g. Suri *et al.* 2017). The simplest example for such complex state space attractors is the robust heteroclinic cycle between two weakly unstable instances of symmetry related OWR described in RS19.

In case 3, invariant states do not exist at specific control parameters but their pattern is reminiscent in some state space regions that may be transiently visited by the dynamics. Folds or symmetry-breaking bifurcations may limit the existence of invariant states in parameter space. However, the pattern of the invariant state may still emerge transiently at control parameters beyond the existence limits. We have observed this case for the transient skewed varicose pattern along a dynamical connection from unstable to stable straight convection rolls in Rayleigh-Bénard convection (Section 3.1), as well as for transient subharmonic oscillations at $[\epsilon, \gamma] = [1.5, 17°]$ (see Section 4.2.1 in RS19) where the SSW-branch does not exist anymore due to a fold (Figure 6). The state space structure supporting such transient dynamics seems related to a state space structure supporting intermittency (Pomeau & Manneville 1980).

Consequently, the patterns of invariant states are often observed because invariant states are stable and attracting, but neither stability nor existence of invariant states is required for observing their pattern.

4.1. *Bifurcation types (Q1)*

Bifurcations create or destroy invariant states and change the stability along state branches. Thus, bifurcation structures describe how state space structures change across control parameters. In response to question $Q1$, stated in the introduction, we list all the different types of bifurcations found in the present study and refer to particular examples. Identified bifurcation types include:

Pitchfork bifurcation, e.g. from TR or LR to KN along ϵ at $\gamma = 80°$ (Figure 11). Equivariant pitchfork bifurcation, e.g. from B to RB and OR along ϵ at $\gamma = 40°$ (Figure 10). Hopf bifurcation, e.g. from TR to TO along ϵ at $\gamma = 100°$ (Figure 12). Equivariant Hopf bifurcation, e.g. from LR to SSW and STW along γ at $\epsilon = 1.5$ (Figure 6). Saddle-node bifurcation, e.g. WR along ϵ at $\gamma = 90°$ (Figure 3, panel $\gamma = 90°$). Mutual annihilation of two periodic orbits, e.g. the two folds bounding the SSW isola along γ at $\epsilon = 0.5$ (Figure 4). The global bifurcation of a periodic orbit colliding with a structurally robust heteroclinic cycle, e.g. the SSW collision with $TR \to \tau_x TR \to TR$ along Ra at $\gamma = 10°$ (Figure 8).

The symmetry-breaking pitchfork and Hopf bifurcations are found as ϵ- or γ-forward or backward bifurcations. The orientation of bifurcations can change when control param-

eters are changed, e.g. WR bifurcates γ-forward from LR at $\epsilon = 0.1$, but γ-backward at $\epsilon = 0.5$ (Figure 4). Moreover, pitchfork and Hopf bifurcations can be supercritical or subcritical independent of their orientation. The ϵ-backward pitchfork bifurcation from $R_{\lambda 2}$ to SV at $\gamma = 0°$ is subcritical (Figure 5) but the ϵ-backward pitchfork bifurcation from OR to DWR at $\gamma = 40°$ is supercritical (Figure 9f).
The sequential order in which bifurcations occur may depend on the considered path through parameter space. RB at $\epsilon = 0.5$ for example can bifurcate in primary or secondary bifurcations along γ. When decreasing γ towards $\gamma = 46°$, RB bifurcate from B in a primary bifurcation. When increasing γ towards $\gamma = 24°$, RB bifurcate from TR in a secondary bifurcation (Figure 4, panel $\epsilon = 0.5$). Thus, describing for example WR as tertiary state implies a particular parameter path. Since WR can bifurcate from RB that may be described as tertiary state (Figure 3, panel $\gamma = 50°$), WR may also be described as quartenary state.

The relation between bifurcation structures and spatio-temporally complex dynamics is in general complicated. The various local and global bifurcations can modify the coexisting invariant states and their dynamical connections in various ways. Coexistence of invariant states may result from supercritical or subcritical bifurcations as well as from folds. These bifurcation types exist in ILC at all angles of inclinations. For example, the subcritical coexistence of stable straight convection rolls with unstable SV (Figure 5) or with unstable SSW (Figure 3, panels $\gamma = 10°, 20°$), supports the experimental observation of spatially localized variants of these spatially periodic states (Bodenschatz *et al.* 2000; Daniels *et al.* 2000). The supercritical coexistence of WR with DWR, OR or OWR (Figure 9) supports the observed pattern defects within the spatially coexisting wavy rolls of different orientations (Daniels & Bodenschatz 2002). The details of these relations are non-trivial as they require to consider spatial dynamics (e.g. Knobloch 2015).

For a specific bifurcation structure we see a generic relation to complex temporal dynamics. All computed sequences of primary and secondary supercritical ϵ-forward pitchfork or Hopf bifurcations give rise to one of the four sequences of dynamical connections. These are $B \rightarrow LR \rightarrow SSW, WR$ and $B \rightarrow TR \rightarrow KN, TO$ as observed in RS19 and illustrated in Figure 2. Consequently, a 'sequence of bifurcations' (Busse & Clever 1996), that consists of supercritical ϵ-forward bifurcations, gives rise to a corresponding 'sequence of dynamical connections'.

4.2. *Connection to instabilities (Q2)*

The patterns of the tertiary invariant states SV, SSW/W, WR, KN and TO are similar to the pattern motifs associated to the five secondary instabilities in ILC at Pr = 1.07 (Subramanian *et al.* 2016). The similarity suggests that the invariant states bifurcate at corresponding secondary instabilities. To confirm this, we compare the bifurcation points of the nonlinear state branches with the critical threshold parameters of the secondary instabilities determined by Subramanian *et al.* (2016) using Floquet analysis (compare with question $Q2$ stated in the introduction). Floquet analysis solves for the pattern wavelengths that first become unstable at the critical threshold ϵ_c when ϵ is increased towards ϵ_c for fixed γ. For numerical continuation of invariant states, the pattern wavelength is prescribed. The critical threshold ϵ_c is determined by continuing the state branch down in ϵ towards the bifurcation at ϵ_c for fixed γ. Consequently, Floquet analysis yields the minimal ϵ_c of the instability, while branches of invariant states at prescribed wavelengths bifurcate at higher ϵ_c. We expect comparable critical thresholds between the two methods if the associated pattern wavelengths are comparable.

Table 1 compares the results of Floquet analysis and bifurcation analysis in terms of pattern wavelengths L_x and L_z, critical thresholds ϵ_c, and critical frequency ω_c for Hopf

Table 1: Comparison between critical thresholds of secondary instabilities determined by Floquet analysis (Subramanian *et al.* 2016) and the critical bifurcation points determined by the present bifurcation analysis. The comparison requires to state all critical frequencies $\omega_c^\dagger$ in diffusion time scales. Frequencies in free fall time units, used throughout this paper series, are obtained via $\omega = \omega^\dagger/\sqrt{PrRa}$.

	Floquet analysis				**bifurcation analysis**			
γ	instability	(L_x, L_y)	ϵ_c	$\omega_c^\dagger$	invariant state	(L_x, L_y)	ϵ_c	$\omega_c^\dagger$
0°	skewed varicose	(10.6, 8.07)	1.100	0	SV	(8.88, 8.06)	1.020	0
10°	long. subh. oscil.	(4.89, 4.03)	1.360	6.211	SSW/TW	(4.44, 4.03)	1.454	6.269
20°	long. subh. oscil.	(4.89, 4.03)	0.900	11.66	SSW/TW	(4.44, 4.03)	0.929	11.64
20°	wavy	(62.8, 2.02)	0.018	0	WR	(4.44, 2.02)	0.054	0
30°	wavy	(62.8, 2.02)	0.014	0	WR	(4.44, 2.02)	0.033	0
40°	wavy	(62.8, 2.02)	0.013	0	WR	(4.44, 2.02)	0.034	0
50°	wavy	(62.8, 2.02)	0.013	0	WR	(4.44, 2.02)	0.043	0
60°	wavy	(62.8, 2.02)	0.013	0	WR	(4.44, 2.02)	0.072	0
70°	wavy	(62.8, 2.02)	0.013	0	WR	(4.44, 2.02)	0.159	0
80°	knot	(2.23, 2.03)	0.026	0	KN	(2.22, 2.02)	0.024	0
90°	trans. oscil.	(26.9, 13.4)	0.063	1.733	TO	(26.7, 12.1)	0.061	2.527
100°	trans. oscil.	(27.2, 15.7)	0.060	1.484	TO	(26.7, 12.1)	0.060	2.776
110°	trans. oscil.	(27.4, 17.0)	0.057	1.312	TO	(26.7, 12.1)	0.059	3.043

bifurcations. We find clear agreement between the results for skewed varicose, longitudinal subharmonic oscillatory, and knot instabilities. Note that Floquet analysis finds the skewed varicose instability for $\gamma = 0°$ at a slightly higher ϵ_c than the bifurcation analysis. This suggests that the Floquet analysis did not capture the most unstable wavelengths of the skewed varicose instability.

For the wavy instabilities, the ϵ_c obtained from the bifurcation analysis is significantly larger. This discrepancy results from the difference in wavelength L_x. Floquet analysis indicates L_x one order of magnitude larger than the L_x prescribed in the bifurcation analysis. We confirmed that WR bifurcates at identical ϵ_c when identical pattern wavelengths are prescribed. Thus, the equilibrium state WR bifurcates at the previously characterised wavy instability.

For the transverse oscillatory instability, the two methods agree in ϵ_c but differ in the critical frequency ω_c. The reasons for this discrepancy are not clear. Continuing the periodic orbit TO to identical pattern wavelengths does not change the critical frequency much. Thus, we hypothesise that the instability characterised by Floquet analysis corresponds to a different bifurcating periodic orbit as TO. This hypothesis is supported by two observations. First, a weakly nonlinear analysis of the normal form near the transverse oscillatory instability suggests a subcritical ϵ-backward bifurcation. TO however, is always found to bifurcate supercritically and ϵ-forward. Second, the pattern of TO can be described as spatially subharmonic standing wave oscillations. Like the subharmonic standing wave state SSW, also TO oscillates on the time scale of the laminar mean advection across the pattern $L_x/\bar{U}_0$ (Section 2.1). Thus, these subharmonic standing waves satisfy the approximate resonance condition

$$m\, L_x\, \omega_c \approx n\, \bar{U}_0 2\pi \ , \tag{4.1}$$

with $(m, n) \in \mathbb{N}$. For bifurcations to SSW at small γ, this approximation holds for $(m, n) = (2, 1)$ with relative errors of about $\pm 15\%$. The nonlinear time scales along the

SSW-branch are shown in Figure 6d. For bifurcations to TO, this approximation holds for $(m, n) = (2, 1)$ with relative errors of less than $\pm 10\%$. The nonlinear time scales along the TO-branch are shown in Figure 12e. The transverse oscillatory instability from Floquet analysis however satisfies (4.1) best for $(m, n) = (4, 1)$. Due to the different resonance numbers, we suspect other physics than those of subharmonic standing waves to govern the instability described by Floquet analysis. Future research should investigate the possibility for other periodic orbits than TO to bifurcate, possibly subcritically, at or near the transverse oscillatory instability. Except in the case of TO, the bifurcating invariant states match the characteristics of the secondary instabilities described previously in Subramanian *et al.* (2016).

4.3. *Range of existence (Q3)*

The third specific question is about the limits of existence of invariant solutions as control parameters are varied (*Q3* state in the introduction). This problem has been approached by continuing invariant states as far as possible along *a priori* defined sections across the $[\gamma, \epsilon]$-parameter space at $\mathrm{Pr} = 1.07$. Since the continuation methods allow tracing invariant states beyond critical threshold parameters of additional instabilities, it was possible to follow bifurcation branches over large intervals of control parameters. The travelling wave STW, for example, is found to exist over a large range of inclinations $10^\circ \leqslant \gamma \leqslant 110^\circ$, covering different flow regimes with small and large laminar shear forces. We identify three invariant states SSW/W and WR whose solution branches persist across the angle of the codimension-2 point γ_{c2}, and for $\gamma > 90^\circ$ where their parent state LR has disappeared. With the exception of SV, all tertiary invariant states are found to exist for the case of vertical convection with $\gamma = 90^\circ$. All invariant states existing at $[\gamma, \epsilon] = [90^\circ, 1.5]$ are briefly discussed and compared with turbulent vertical convection in Appendix B. We visually summarise the regions of existence and coexistence of the computed invariant states in Figure 13.

Continuation and stability analysis along state branches revealed bifurcations to or from other invariant states. These states are neither clearly observed in experiments or simulations, nor do they correspond to instabilities found by Floquet analysis. The stability analysis along the branch of WR (Section 3.3) introduced four additional equilibrium states, namely DWR, OR, OWR, and RB. Other invariant states were obtained because continuations terminated at bifurcations from these states. Specifically, TO may bifurcate from the TSV equilibrium (Figure 4, $\epsilon = 0.1$), KN may bifurcate from SL (Figure 3, $\gamma = 90^\circ$), and a global bifurcation of SSW may involve LSV as parent state (Figure 6c). These three additional states are described in Appendix A. We do not distinguish invariant states connected via folded bifurcation branches as upper and lower branch states. Folds exist at all angles of inclinations. See e.g., the bifurcation branches of SV at $\gamma = 0^\circ$, and of STW at $\gamma = 110^\circ$. However, we observe that state branches tend to become more folded towards inclinations around vertical (compare panels in Figure 3).

5. Conclusions

The present bifurcation analysis has identified an extensive network of parametrically connected invariant state branches in inclined layer convection. Overall, 16 different nonlinear three-dimensional invariant states have been discussed in the present article. Many of them are related to spatio-temporally complex dynamics observed in experiments and simulations. Seven different types of bifurcations were found, including common types like Hopf bifurcations or saddle-node bifurcations, and including less common types like equivariant bifurcations or global collisions between periodic orbits and robust hetero-

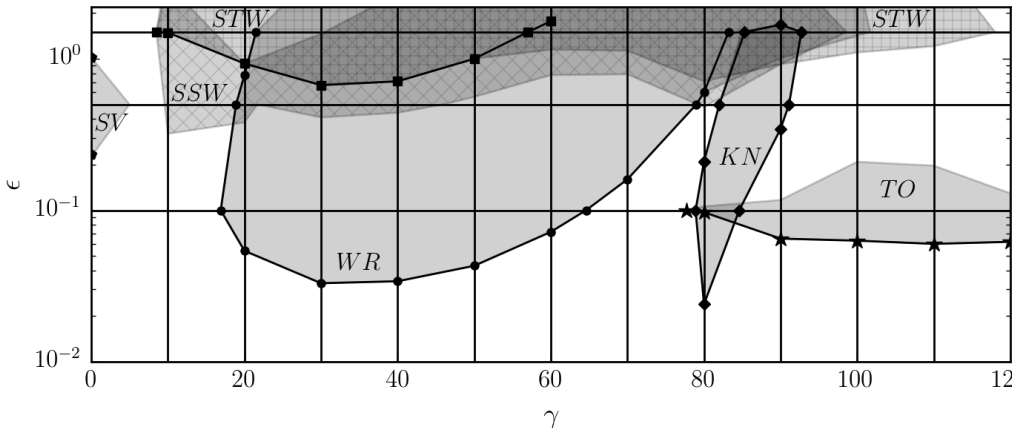

Figure 13: Existence regions of invariant states in the considered parameter space at $\mathrm{Pr} = 1.07$. Local symmetry breaking bifurcations are marked and connected to guide the eye: SV ($\pentagon$), WR ($\circ$) and KN ($\Diamond$) bifurcate in pitchfork bifurcations. SSW/STW ($\square$) and TO ($\star$) bifurcate in Hopf bifurcations. Where existence is not limited by symmetry breaking bifurcations, the limits are due to folds, global bifurcations or, in the case of TO, due to numerical challenges. Hatched regions of existence allow to better distinguish SSW ($\times$) and STW ($+$).

clinic cycles. Computing this many different invariant states and branches just for this work and RS19 has been straightforward relative to recent integrated efforts of the research community to compute similar numbers of invariant states and branches in other canonical shear flows like plane Couette or pipe flow. Inclined layer convection covers flows from horizontal Rayleigh-Bénard convection to vertical layer convection which are relevant for engineering applications and which have been widely studied using experiments and simulations. This article demonstrates that these flows are numerically accessible to nonlinear dynamical systems concepts.

Declaration of Interests

The authors report no conflict of interest.

REFERENCES

Argyris, J., Faust, G. & Haase, M. 1993 Routes to chaos and turbulence. A computational introduction. *Philosophical Transactions - Royal Society of London, A* **344** (1671), 207–234.

Bergeon, A. & Knobloch, E. 2002 Natural doubly diffusive convection in three-dimensional enclosures. *Physics of Fluids* **14** (9), 3233–3250.

Bodenschatz, E., Pesch, W. & Ahlers, G. 2000 Recent Developments in Rayleigh-Bénard Convection. *Annual Review of Fluid Mechanics* **32** (1), 709–778.

Busse, F. H. 1978 Non-linear properties of thermal convection. *Reports on Progress in Physics* **41** (12), 1929.

Busse, F. H. & Clever, R. M. 1979 Instabilities of convection rolls in a fluid of moderate Prandtl number. *Journal of Fluid Mechanics* **91** (02), 319.

Busse, F. H. & Clever, R. M. 1992 Three-dimensional convection in an inclined layer heated from below. *J. Eng. Math.* **26** (1), 1–19.

Busse, F. H. & Clever, R. M. 1996 The sequence-of-bifurcations approach towards an understanding of complex flows. In *Mathematical Modeling and Simulation in Hydrodynamic Stability* (ed. D. N. Riahi), pp. 15–34. World Scientific.

Busse, F. H. & Clever, R. M. 2000 Bursts in Inclined Layer Convection. *Phys. Fluids* **12** (8), 2137–2140.

Busse, F. H. & Whitehead, J. A. 1974 Oscillatory and collective instabilities in large Prandtl number convection. *Journal of Fluid Mechanics* **66** (1), 67–79.

Chen, Y.-M. & Pearlstein, A. J. 1989 Stability of free-convection flows of variable-viscosity fluids in vertical and inclined slots. *Journal of Fluid Mechanics* **198**, 513.

Chossat, P. & Iooss, G. 1994 *The Couette-Taylor Problem*, , vol. 102. Springer.

Clever, R. M. 1973 Finite Amplitude Longitudal Convection Rolls in an Inclined Layer. *Journal of Heat Transfer* **95** (3), 407.

Clever, R. M. & Busse, F. H. 1977 Instabilities of longitudinal convection rolls in an inclined layer. *J . Fluid Mech* **81**, 107–127.

Clever, R. M. & Busse, F. H. 1992 Three-dimensional Convection in a Horizontal Fluid Layer Subjected to a Constant Shear. *Journal of Fluid Mechanics* **234**, 511–527.

Clever, R. M. & Busse, F. H. 1995 Tertiary and Quarternary Solutions for Convection in a Vertical Fluid Layer Heated From the Side. *Chaos Solitons Fractals* **5** (10), 1795–1803.

Cross, M. & Greenside, H. 2009 *Pattern Formation and Dynamics in Nonequilibrium Systems*. Cambridge University Press.

Daniels, K., Plapp, B. & Bodenschatz, E. 2000 Pattern Formation in Inclined Layer Convection. *Physical Review Letters* **84** (23), 5320–5323.

Daniels, K. E. & Bodenschatz, E. 2002 Defect turbulence in inclined layer convection. *Physical review letters* **88** (3), 034501.

Daniels, K. E., Brausch, O., Pesch, W. & Bodenschatz, E. 2008 Competition and bistability of ordered undulations and undulation chaos in inclined layer convection. *Journal of Fluid Mechanics* **597**, 261–282.

Daniels, K. E., Wiener, R. J. & Bodenschatz, E. 2003 Localized transverse bursts in inclined layer convection. *Physical review letters* **91** (11), 114501.

Dijkstra, H. A., Wubs, F. W., Cliffe, A. K., Doedel, E., Hazel, A. L., Lucarini, V., Salinger, A. G., Phipps, E. T., Sanchez-Umbria, J., Schuttelaars, H., Tuckerman, L. S. & Thiele, U. 2014 Numerical Bifurcation Methods and their Application to Fluid Dynamics: Analysis beyond Simulation. *Communications in Computational Physics* **15** (1), 1–45.

Eckhardt, B., Schneider, T. M., Hof, B. & Westerweel, J. 2007 Turbulence transition in pipe flow. *Annual Review of Fluid Mechanics* **39** (1), 447–468.

Fujimura, K. & Kelly, R. E. 1993 Mixed mode convection in an inclined slot. *Journal of Fluid Mechanics* **246**, 545–568.

Gershuni, G. Z. & Zhukhovitskii, E. M. 1969 Stability of plane-parallel convective motion with respect to spatial perturbations. *Prikl. Mat. i Mekh.* **33** (5), 855–860.

Gibson, J. F., Halcrow, J. & Cvitanović, P. 2008 Visualizing the geometry of state space in plane Couette flow. *Journal of Fluid Mechanics* **611**, 107–130.

Gibson, J. F., Reetz, F., Azimi, S., Ferraro, A., Kreilos, T., Schrobsdorff, H., Farano, M., Yesil, A. F., Schütz, S. S., Culpo, M. & Schneider, T. M. 2019 Channelflow 2.0. *in preparation* .

Golubitsky, M. & Stewart, I. 2002 *The Symmetry Perspective*. Springer.

Guckenheimer, J. & Holmes, P. 1983 *Nonlinear oscillations, dynamical systems and bifurcations of vector fields*, *Applied Mathematical Sciences*, vol. 42. Springer-Verlag.

Hart, J. E. 1971 Transition to a wavy vortex régime in convective flow between inclined plates. *Journal of Fluid Mechanics* **48** (2), 265–271.

Juniper, M. P. & Sujith, R. 2018 Sensitivity and Nonlinearity of Thermoacoustic Oscillations. *Annual Review of Fluid Mechanics* **50** (1), 661–689.

Kawahara, G., Uhlmann, M. & van Veen, L. 2012 The significance of simple invariant solutions in turbulent flows. *Annual Review of Fluid Mechanics* **44** (1), 203–225.

Kerswell, R. R. 2005 Recent progress in understanding the transition to turbulence in a pipe. *Nonlinearity* **18** (6), R17–R44.

Knobloch, E. 1986 Oscillatory convection in binary mixtures.

Knobloch, E. 2015 Spatial Localization in Dissipative Systems. *Annual Review of Condensed Matter Physics* **6** (1), 325–359.

Krupa, M. 1997 Robust Heteroclinic Cycles. *Journal of Nonlinear Science* **7** (2), 129–176.

Krupa, M. & Melbourne, I. 1995 Asymptotic stability of heteroclinic cycles in systems with symmetry. *Ergodic Theory and Dynamical Systems* **15** (1), 121–147.

Lenton, T. M., Held, H., Kriegler, E., Hall, J. W., Lucht, W., Rahmstorf, S. & Joachim, H. 2008 Tipping elements in the Earth's climate system. *Proceedings of the National Academy of Sciences* **105** (6), 1786–1793.

Lorenz, E. N. 1963 Deterministic Nonperiodic Flow. *Journal of the Atmospheric Sciences* **20** (2), 130–141.

Mizushima, J. & Tanaka, H. 2002*a* Transition Routes of Natural Convection in a Vertical Fluid Layer. *Journal of the Physical Society of Japan* **71** (12), 2898–2906.

Mizushima, J. & Tanaka, H. 2002*b* Transitions of natural convection in a vertical fluid layer. *Physics of Fluids* **14**.

Pinter, A., Lücke, M. & Hoffmann, C. 2006 Competition between traveling fluid waves of left and right spiral vortices and their different amplitude combinations. *Physical Review Letters* **96** (4), 1–4.

Pomeau, Y. & Manneville, P. 1980 Intermittent Transition to Turbulence in Dissipative Dynamical Systems. *Communications in Mathematical Physics* **74**, 189–197.

Reetz, F. & Schneider, T. M. 2019 Invariant states in inclined layer convection. Part 1. Temporal transitions along dynamical connections between invariant states. *arXiv* .

Ruth, B. D. W., Hollands, K. G. T. & Raithby, A. N. D. G. D. 1980 On free convection experiments in inclined air layers heated from below. *Journal of Fluid Mechanics* **96** (3), 461–479.

Sanchez, J., Net, M., Garcia-Archilla, B. & Simo, C. 2004 NewtonKrylov continuation of periodic orbits for NavierStokes flows. *Journal of Computational Physics* **201** (1), 13–33.

Schaeffer, D. G. & Cain, J. W. 2016 *Ordinary Differential Equations: Basics and Beyond*, , vol. 65.

Subramanian, P., Brausch, O., Daniels, K. E., Bodenschatz, E., Schneider, T. M. & Pesch, W. 2016 Spatio-temporal patterns in inclined layer convection. *Journal of Fluid Mechanics* **794**, 719–745.

Suri, B., Tithof, J., Grigoriev, R. O. & Schatz, M. F. 2017 Forecasting Fluid Flows Using the Geometry of Turbulence. *Physical Review Letters* **118** (11), 1–5.

Tagg, R., Edwards, W. S., Swinney, H. L. & Marcus, S. 1989 Nonlinear standing waves in Couette-Taylor flow. *Physical Review A* **39** (7), 3734–3738.

Tuckerman, L. S. & Barkley, D. 1990 Bifurcation analysis of the Eckhaus instability. *Physica D: Nonlinear Phenomena* **46** (1), 57–86.

Vest, C. M. & Arpaci, V. S. 1969 Stability of natural convection in a vertical slot. *Journal of Fluid Mechanics* **36** (01), 1.

Viswanath, D. 2007 Recurrent motions within plane Couette turbulence. *Journal of Fluid Mechanics* **580**, 339–358.

Waleffe, F. 1997 On a self-sustaining process in shear flows. *Physics of Fluids* **9** (June 1996), 883.

Waleffe, F., Boonkasame, A., Smith, L. M., Waleffe, F., Boonkasame, A. & Smith, L. M. 2015 Heat transport by coherent Rayleigh-Bénard convection Heat transport by coherent Rayleigh-Bénard convection. *Physics of Fluids* **051702** (May).

Weiss, S., Seiden, G. & Bodenschatz, E. 2012 Pattern formation in spatially forced thermal convection. *New Journal of Physics* **053010**, 14; 053010.

Appendix A. Additional invariant states participating in bifurcations

This section briefly discusses three additional invariant states that do not represent previously observed convection patterns at $\mathrm{Pr} = 1.07$ but that participate in the bifurcation network by bifurcating to the above discussed invariant states.

The γ-continuation of SSW at $\epsilon = 1.5$ approaches an equilibrium state at $\gamma = 1.9°$ that we name LSV, short for longitudinal subharmonic varicose state. The pattern of the equilibrium resembles an instance in time along the orbit SSW at $\gamma = 15°$ (Figure 14a). LSV is invariant under transformations of $S_{\mathrm{ssw}} = \langle \pi_{xyz}, \tau(0.5, 0.5) \rangle$ and can be

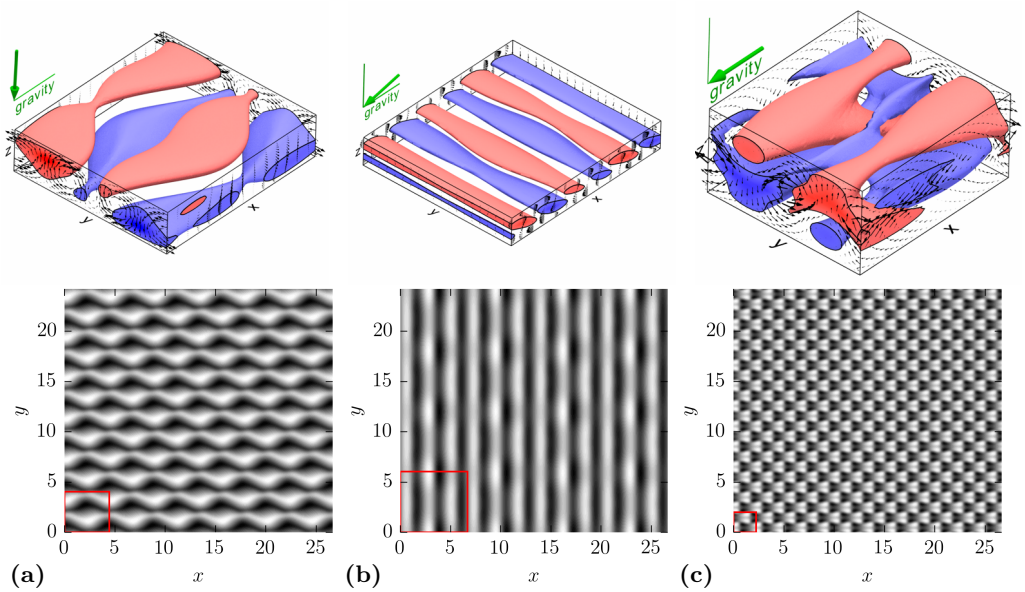

Figure 14: 3D flow structure and midplane temperature contours of three steady equilibrium states participating in bifurcations. **(a)** longitudinal subharmonic varicose LSV, **(b)** transverse subharmonic varicose TSV, **(c)** subharmonic lambda plumes SL.

continued from $\gamma = 0°$ to $\gamma = 30°$ along which the relative position of the hot and cold plumes changes continuously.

Just below γ_{c2}, a γ-forward Hopf bifurcation generates TO from an equilibrium state, previously named transverse subharmonic varicose (TSV), at $\epsilon = 0.1$ (inset panel in Figure 4). This invariant state represents stationary varicose modulations of the TR pattern with $[3\lambda_x, 3\lambda_y]$-periodicity and invariance under transformations of $S_{\mathrm{tv}} = \langle \pi_{xz}, \pi_y \rangle$ (Figure 14b). TSV are similar to the state discussed in Clever & Busse (1995) but have different periodicity.

Due to the absence of LR at finite Ra at $\gamma = 90°$, KN do not terminate in a bifurcation from LR as described in Section 3.4 but from SL, an equilibrium that we name subharmonic lambda plumes. The $[\lambda_x, \lambda_y]$-periodic SL emerges in a saddle-node bifurcation at $\epsilon = 1.670$. From the upper branch of SL, KN bifurcate ϵ-backward at $\epsilon = 1.672$ (Figure 3). The subharmonic flow structure of SL is invariant under transformations of $S_{\mathrm{sl}} = \langle \pi_{xz}\tau(0, 0.5), \pi_y\tau(0.5, 0), \tau(0.5, 0.5) \rangle$ and resembles lambda-shaped plumes at scales of half the gap height (Figure 14c).

Appendix B. Invariant states in vertical layer convection

ILC at $\gamma = 90°$ is a particular case because vertical layer convection has the largest laminar shear forces of all inclinations and can be considered a pure shear flow. Here, buoyancy provides a body force along the channel domain, acting like a pressure gradient in pressure-driven channel flow. Despite the absence of a wall-normal buoyancy force, all main invariant states considered in the present study were numerically continued to $\gamma = 90°$, with the exception of LR existing only at $\mathrm{Ra} = \infty$ due to (3.2-3.6) and SV. The flow structures of the invariant states at $\gamma = 90°$ and $\epsilon = 1.5$ show sharper interfaces and

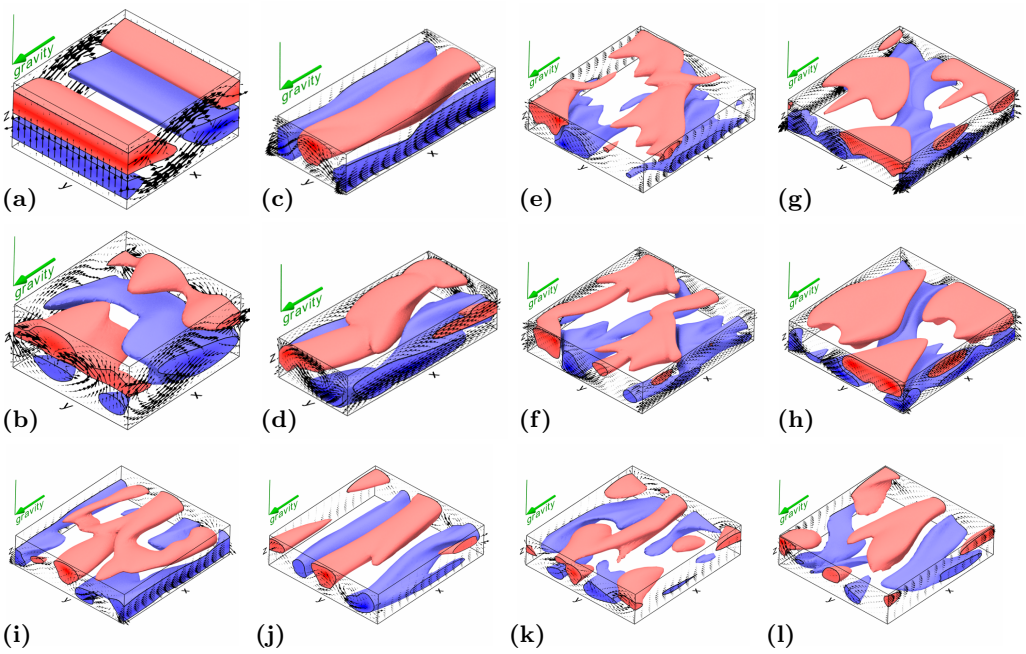

Figure 15: Continuation yields eight invariant states in vertical layer convection ($\gamma = 90°$) at $\epsilon = 1.5$ (Ra = 21 266). **(a)** TR, **(b)** KN, **(c/d)** upper/lower branch of WR, **(e/f)** upper/lower branch of SSW, **(g/h)** upper/lower branch of STW. The distinction between upper/lower branches refers to $||\theta||_2$. The upper branches of WR and SSW are closer to bifurcations from LR than the lower branches, for STW *vice versa*. **(i)-(l)** Snapshots from a DNS at $\gamma = 90°$ and $\epsilon = 1.5$ show transiently emerging structures resembling the invariant states above.

more pointed convective plumes than at the parameters where these states were initially found (Figure 15).